Stochastic Environmental Research and Risk Assessment
https://doi.org/10.1007/s00477-025-02990-6

ORIGINAL PAPER

Anthropogenic heat effects on local deviations from the global mean annual air temperature: a case study of Modena, Italy

Isabella Morlini[1] · **Stefano Orlandini**[2]

Accepted: 11 April 2025

Abstract

Global mean surface air temperature is a key metric in climatology, but understanding its relationship with local temperatures is crucial for projecting climate impacts at regional and local scales. This study analyzes air temperature data from Modena, Italy, in comparison with NASA GISTEMP global mean annual air temperature for the period 1881–2021 to identify local deviations from global patterns and assess the interplay of local and global factors influencing urban temperatures. Since linear relationships are found to be spurious, nonlinear methods such as cubic splines and regression trees are employed. Cubic splines effectively capture asymmetric bivariate relationships between local temperature deviations and influencing factors without overfitting, while regression trees highlight the most influential predictors in multivariate analysis. The analysis shows that both local and global temperatures are strongly correlated with global CO_2 concentrations. However, deviations arise due to local factors such as urban expansion and variations in precipitation. Since 1986, the increasing number of registered vehicles appears to contribute significantly to these deviations, likely through traffic congestion and resulting anthropogenic heat. Although further research is needed for reliable validation, an order-of-magnitude analysis supports the plausibility of this hypothesis. The findings suggest that urban areas may experience a 'fever' from anthropogenic heat effects. Targeted mitigation strategies, such as reducing traffic congestion, could help address these localized impacts.

Keywords Local air temperature · CO_2 concentration · Urban area expansion · Anthropogenic heat · Vehicle impact

1 Introduction

It is widely recognized that global warming has become an undeniable challenge significantly affecting human existence and global social development (Wu et al. 2016). The NASA Goddard Institute for Space Studies (GISS) Surface Temperature Analysis (GISTEMP v4) provides Earth and space scientists with estimates of global mean surface air temperature changes (GISTEMP Team 2021; Lenssen et al. 2019). These changes are evaluated relative to the average temperature during the 1951–1980 base period (GISTEMP Team 2021). Global temperature is closely linked to atmospheric CO_2 concentrations, highlighting the significant impact of global development on climate (Hansen et al. 1981; Jones et al. 1999; Jouzel et al. 2007; Lüthi et al. 2008; Milly et al. 2008). Recent studies, however, emphasize emerging deviations between observed local temperatures and estimated global temperatures (Sutton et al. 2015). Over the past few decades, surface temperatures have risen notably in urbanized cities worldwide, leading to the phenomenon known as the "urban heat island" (Arnfield 2003; Rizwan et al. 2008; Rachma and Lin 2024). The physical processes underlying the urban heat island effect and urban climate in general have been studied, among others, by Nunez and Oke (1977), Oke (1988), Oke et al. (2017), and Chen et al. (2021). Although global mean surface air temperature is a critical metric in climatology (Hansen et al. 2010), it is equally important to investigate the statistical relationship between global and local urban temperatures. Internal climate variability plays a crucial role in projecting climate impacts on regional and local scales (Chen et al. 2009; Sutton et al. 2015; Al-Sakkaf et al. 2024).

✉ Isabella Morlini
isabella.morlini@unimore.it

[1] Dipartimento di Comunicazione ed Economia, Università degli Studi di Modena e Reggio Emilia, Reggio Emilia, Italy

[2] Dipartimento di Ingegneria Enzo Ferrari, Università degli Studi di Modena e Reggio Emilia, Modena, Italy

Beyond deterministic studies of the physical processes underlying the urban heat island effect and urban climate, statistical analysis of long-term observational records can validate or challenge hypotheses derived from modeling efforts (De Munck et al. 2013; Salamanca et al. 2014; Sutton et al. 2015; Yu et al. 2021). Such analyses can evaluate the role of local factors in urban heat islands, offering insights for mitigating their causes. Urban climatology, in fact, may benefit from studies that move beyond process-based research and simulation modeling toward statistical analysis, thereby enhancing the explanatory power available to urban climatologists. Since a long-term air temperature record is available from the city center of Modena, Italy, this study investigates the relationship between local and global mean annual air temperatures, with a particular focus on significant local deviations from the global mean observed over the past two decades. Because the study centers on these deviations, the global NASA GISTEMP data are preferred over the gridded GISTEMP dataset, which inherently includes local effects (Lenssen et al. 2024). The gridded dataset is available at a resolution of $1° \times 1°$, or roughly 111 km × 111 km. In the study area, it is difficult, if not impossible, to identify grid cells of this size that represent purely urban or purely rural environments. Most cells contain a mix of cities, towns, and densely populated rural areas. Therefore, this study does not attempt to compare urban and rural temperatures. Rather, it focuses on analyzing long-term local temperature records collected in an urban setting and comparing them to global temperatures that reflect average conditions across mixed land-use regions (Hausfather et al. 2013). This study does not make any projections. Instead, it presents a statistical analysis of observed local temperatures alongside widely accepted GISTEMP global data. The analysis aims to highlight the significance of local temperature trends in relation to the GISTEMP global series, which is interpreted as a representation of an underlying global signal. More specifically, it addresses the question: How do anthropogenic heat sources influence local deviations from the global mean annual air temperature in Modena?

The analysis focuses on a long-term dataset (1881–2021) of mean annual air temperature T, representing local temperature, and annual precipitation depth P, a potentially related climatic variable, both observed in Modena. These are analyzed alongside data on urban area extent A, observed or reconstructed for Modena, as a potential indicator of local development. A projection of global temperature for Modena is derived by adding the average temperature observed in Modena during the 1951–1980 base period to the GISTEMP global surface temperature change (GISTEMP Team 2021; Lenssen et al. 2019). This is a standard methodology for estimating absolute temperature time series from anomaly data (e.g., Brohan et al. 2006; Hansen et al. 2010; Rao et al. 2018). Additionally, global CO_2 concentration, obtained from ice core records (starting in 1881) and Mauna Loa observations (from 1959), is included as a variable representative of global development (Etheridge et al. 1998; National Oceanic and Atmospheric Administration 2021). Notable deviations between observed local urban air temperatures in Modena and GISTEMP global temperatures are evident throughout the analyzed period, with significant positive deviations particularly prominent in the last two decades. The time series of registered cars M and vehicles V in Modena are used to account for a potential human activity that may contribute to local temperature variations relative to global climate trends. While many studies have estimated the impact of vehicle fleets on air quality (e.g., Cardona-Jiménez et al. 2024; Chauhan and Singh 2020; Gualtieri et al. 2020), little attention has been given to the local-level impact of vehicles on temperature increases. The statistical analysis of local and global mean annual air temperature, along with potentially related variables, is conducted to detect local deviations from global patterns and to explore the combined effects of local and global development on urban air temperature.

Possible explanations for the observed deviations are explored through an analysis of uninterrupted time series for T, P, A, G, and C over the period 1881–2021. In addition, data on registered cars M and vehicles (V) in Modena are available for the years 1986–1998 and 1996–2021. While this dataset does not provide a comprehensive global perspective on the influence of local and global development on urban air temperature, it offers a valuable observational record of long-term relationships among key local and global variables, which are often unavailable in global studies due to the scarcity of extended time series. Although the relationship between G and global CO_2 concentration is well established (Trevin 2016; Zittis et al. 2022), understanding the impact of climatic variables and local development on T remains critical. Assessing the dependence of local urban air temperature increases on potential explanatory variables is challenging for several reasons. First, for annual data, causal directionality between climatic variables is unclear. For example, annual temperature may influence precipitation depth, and vice versa. Second, interactions among development-related variables, such as C and A, complicate modeling. Third, shared increasing trends across variables can affect linear model outcomes. The comparison of linear relationships between original series (which exhibit similar temporal trends) and first-differenced series (devoid of trends) often reveals spuriousness in linear models. To address these challenges, regression trees and cubic splines are employed to analyze complex nonlinear relationships among the observed geophysical variables (Hastie and Tibshirani 1986; Breiman et al. 1984; Morgan and Sonquist 1963). Cubic splines identify the best predictors of T among global and local development and environmental variables, while regression trees provide insights into potential nonlinear relationships and interactions among predictors. Additionally, regression trees detect change points in multivariate dependence structures. Although methods like the Mann–Kendall and Pettitt tests are widely used to identify change points in univariate climatic series, few studies address the detection of multivariate change points (Qian et al. 2024). Identifying such changes in the relationships between temperature patterns and local/global climatic and development variables is crucial for understanding local warming mechanisms and improving development planning and management. The paper is structured as follows: Sect. 2 describes the data and methods, Sect. 3 presents the results of statistical and order-of-magnitude analyses, Sect. 4 discusses the findings, and Sect. 5 concludes with recommendations for mitigating local climate change impacts.

2 Data and methods

2.1 Data

The annual time series of local mean air temperature (T) and cumulative precipitation depth (P) were obtained from uninterrupted daily observations collected since 1861 and 1830, respectively, at the Osservatorio Geofisico di Modena, located inside the city of Modena, Italy (latitude 44°38′53.15″ N, longitude 10°55′47.35″ E, elevation 76.50 m above sea level (asl)). The Osservatorio Geofisico di Modena is situated in the Torre di Levante (eastern tower) of the Palazzo Ducale in Modena, Italy. The observatory is affiliated with the University of Modena and Reggio Emilia and serves as a center for research in meteorology, climatology, and geophysics. It also houses a museum featuring historical scientific instruments and documents. The local series of air temperature and precipitation depth analyzed in this study are particularly valuable, as they are derived from uninterrupted daily observations collected from January 1, 1861, to December 31, 2021. These long-term in situ observations (161 years per series) are not significantly affected by inhomogeneities caused by changes in instrumentation, station relocation, or variations in observing practices, such as different formulas for calculating minimum and maximum values or changes in observation times. As highlighted by Boccolari and Malmusi (2013), the Modena time series benefit from the fact that sensors have been positioned in the same location, the eastern tower of the Palazzo Ducale di Modena, except for a brief period during World War II (1944–1945). Throughout the observation period, sensors have always been monitored by at least one operator. Since 1985, meteorological observations have been conducted daily using automatic equipment. A change in the hygrothermograph, an instrument used to simultaneously measure and record humidity and temperature over time, was made in 1869, prior to the starting year (1881) of the series considered in this study. Additional metadata detailing the station's history can be found in Corradini (2014).

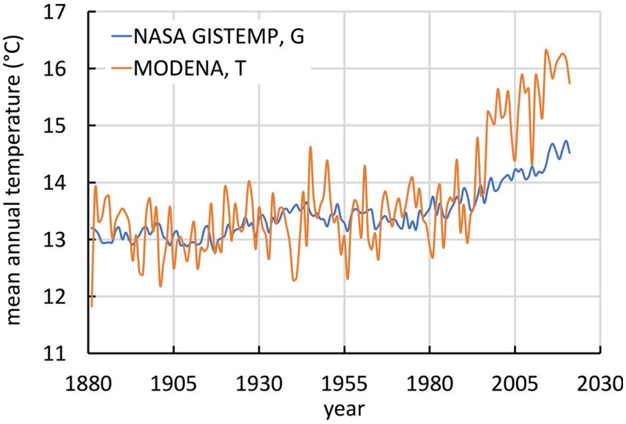

Fig. 1 Comparison between local air temperature observed in Modena (T) and NASA GISTEMP global air temperature (G) estimated by the Goddard Institute for Space Studies (GISS). GISTEMP global air temperature for Modena is obtained by adding the average temperature observed in Modena in the 1951–1980 base period, namely T_b = 13.38 °C, to GISTEMP anomaly data

In this study, we focus on data from 1881 onward to compare the series with selected related variables. The GISTEMP surface temperature series (GISTEMP Land & Ocean Combined) is used as an estimate of global surface temperature change from 1881. A projection of global temperature for Modena (G) is derived by adding the average temperature observed in Modena during the 1951–1980 base period (T_b = 13.38 °C) to the GISTEMP temperature anomalies. This is a standard procedure in climatology that enables a direct comparison between the derived GISTEMP global temperature (G) and the observed local temperature (T) in Modena, as shown in Fig. 1. Although significant internal variability exists in local air temperature on a monthly scale, the long-term trends of T, G, and monthly values of T are similar (Appendix 1, Fig. 18). The present paper focuses on annual values to investigate the long-term relationship, free from the influence of periodic or geographically specific climatic variations. As shown in Fig. 1, the GISTEMP global series (G) and the Modena local series (T) closely align between 1880 and 1990, with notable deviations emerging after 1990. The close agreement between locally observed absolute temperatures and those reconstructed by combining GISTEMP anomalies with local baseline records for the 1951–1980 period is not a given. It relies on the assumption that absolute temperatures remained relatively stable throughout the baseline. The GISTEMP G series represents the global average temperature and, therefore, does not account for the fact that land surfaces warm faster than seas and oceans due to differences in thermal capacity, nor does it consider that different regions of the Earth warm at different rates. However, the close match between global and local temperatures during the period 1880–1990 suggests that regional differences relative to the global GISTEMP do not play a significant role, at least in determining local deviations from the global mean annual air temperature, as analyzed in this study. A visual comparison of the GISTEMP Land & Ocean combined series with the Land-only series confirms that differences in thermal inertia do not significantly account for the local deviations observed over the past two decades (Appendix 2, Fig. 19). Furthermore, because this study focuses on deviations of local temperature from the global mean annual air temperature, the global GISTEMP data (*G*) are preferred over the gridded version, which inherently includes local effects (Appendix 3, Fig. 20).

Observations of the urban area extent (*A*) of Modena are available for the years 1881, 1940, 1961, 1971, 1981, 1998, 2000, and 2002–2021. Cubic spline interpolation is applied to reconstruct values of *A* for the intervening years between 1881 and 2021. Global CO_2 concentration (*C*), estimated from ice cores for the period 1832–1978 and observed at the Mauna Loa Observatory (latitude 19.5362°N, longitude 155.5763°W, elevation 3397.00 m asl), Hawaii, from 1959 onward, is combined to provide an annual time series for 1881–2021 (with ice core data from 1881 to 1958 and Mauna Loa data from 1959 to 2021). With the uninterrupted series of 141 annual values of *T*, *P*, *A*, *G*, and *C* obtained for the period 1881–2021, we create the first dataset. Figure 2 presents a scatter plot matrix that visualizes bivariate relationships among combinations of variables over the 141 years considered. When considering annual values,

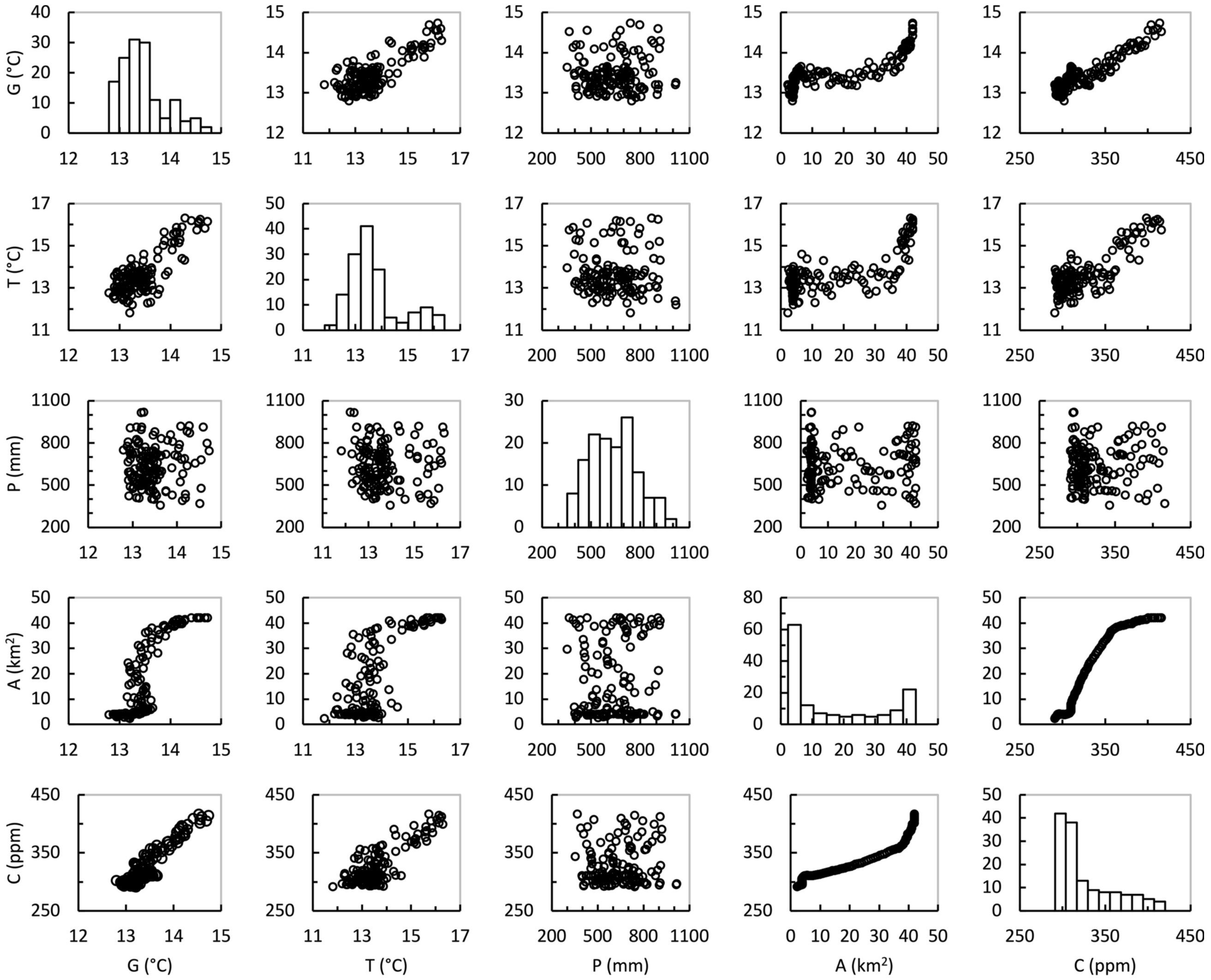

Fig. 2 Scatter plot matrix illustrating the absolute frequency distributions of *T, P, A, G*, and *C* (i.e., the number of occurrences, *n*, over discrete intervals) and their pairwise relationships observed from 1881 to 2021

lagged variables are ineffective predictors of T, and the scatter plot diagrams are useful for highlighting the presence of linear or nonlinear relationships between pairs of variables. The histograms on the diagonal of the scatter plot matrix reveal irregular and asymmetric distributions, which suggest that parametric models are unsuitable for fitting the relationships between variables. From the scatter plot matrix, we observe that some variables are strongly linearly correlated. Symmetric pairwise linear relationships between T, P, A, G, and C in the first dataset are assessed by computing correlation coefficients (r) and their associated p-values for all pairs of variables. Note that correlation analysis is symmetric and does not imply causation; it only measures the strength and direction of the linear relationship between variables, without inferring a cause-and-effect relationship.

Highly significant correlations ($p\text{-value} < 0.01$) exist between T and A, T and G, T and C, A and G, A and C, and G and C, while insignificant correlations ($p\text{-value} > 0.05$) are found between all other pairs of variables involving P (Taylor 1997 p. 290). However, correlations can be spurious due to mutual influence from a third, common, related (confounding) variable. For example, in this study, spurious correlation may arise between variables that both exhibit the same positive trend over time, independent of each other. A detailed analysis of the trends and change points of T, P, A, and C over the period 1881–2119 can be found in Morlini et al. (2024). To identify potential spurious correlations, we compute the first differences (ΔT, ΔP, ΔA, ΔG, ΔC) of the series for T, P, A, G, and C, respectively (Hooker 1905; Aldrich 1995) and evaluate the corresponding linear pairwise relationships. Highly significant correlations ($p\text{-value} < 0.01$) are found only between ΔT and ΔP, and between ΔA and ΔC. A significant correlation ($0.01 \leq p\text{-value} \leq 0.05$) exists between ΔG and ΔC, while insignificant correlations ($p\text{-value} > 0.05$) are found between the other pairs of first differences. The analysis of first differences suggests that the highly significant linear relationships between T and A, T and G, T and C, and A and G are spurious, while the relationships between T and P, A and C, and G and C are likely nonspurious. Since spurious correlations in symmetric linear (correlation) relationships are also expected in asymmetric linear regression models, we perform asymmetric nonlinear regression analysis to investigate the relationships between T, P, A, G, and C.

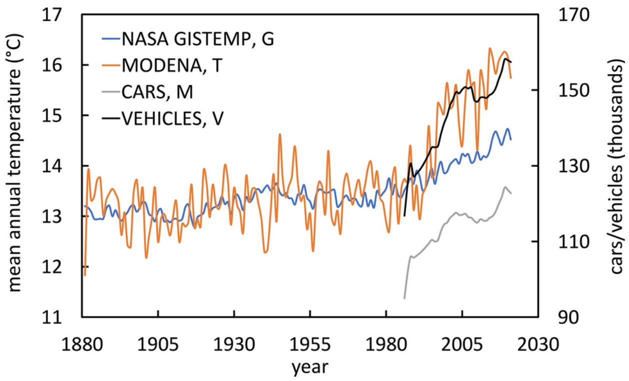

Fig. 3 Time series showing the number of registered cars (M) and vehicles (V) in Modena, along with the NASA GISTEMP global air temperature (G) estimated by the Goddard Institute for Space Studies (GISS), and local air temperature (T) observed in Modena

Observations of registered cars (M) and vehicles (V) in Modena are available for the years 1986–1998 and 1996–2021. To fill in the gaps for the years 1989–1995, we apply cubic spline interpolation and create a second dataset of 36 annual observations for the period 1986–2021, which includes two additional variables related to local development and urbanization. The time series showing the number of registered cars (M) and vehicles (V) in Modena is reported in Fig. 3. In fact, the growth of vehicle fleets in metropolitan areas could be a potential driver of urban heat, alongside urbanization. Figure 4 presents a scatter plot matrix that visualizes bivariate relationships among combinations of variables over the 36 years considered. In this dataset, highly significant correlations ($p\text{-value} < 0.01$) are found only between ΔT and ΔP, ΔA and ΔC, and ΔM and ΔV. Insignificant correlations ($p\text{-value} > 0.05$) are observed between all other pairs of first differences. Notably, in more recent years, the previously significant linear relationship between global temperature and global CO_2 becomes insignificant. Figure 3 shows the time series for G, T, M, and V on the same graphs. The behavior of these series suggests that M, V, and T follow a similar pattern, especially over the last 5 years. This common trend points to the need for a nonlinear analysis of the impact of cars M and vehicles V on local temperature T and its deviations from the global temperature pattern.

2.2 Methods

Cubic spline interpolation is first performed to evaluate and compare asymmetric pairwise relationships, with local temperature (T) considered as the dependent variable and, in turn, local urbanization (A), global CO_2 concentration (C), and local precipitation depth (P) as explanatory variables. When using the second data set, we also include the number of cars (M) and vehicles (V) as explanatory variables. The same analysis is then conducted using the difference DT between T and G as the dependent variable. Spline modeling has become an established tool in statistical regression analysis and is widely used for building explanatory models in many fields of research that require non-linear smooth functions while avoiding distributional assumptions. More importantly, splines offer the advantage of locality, meaning the fitted function at a given value does not depend on

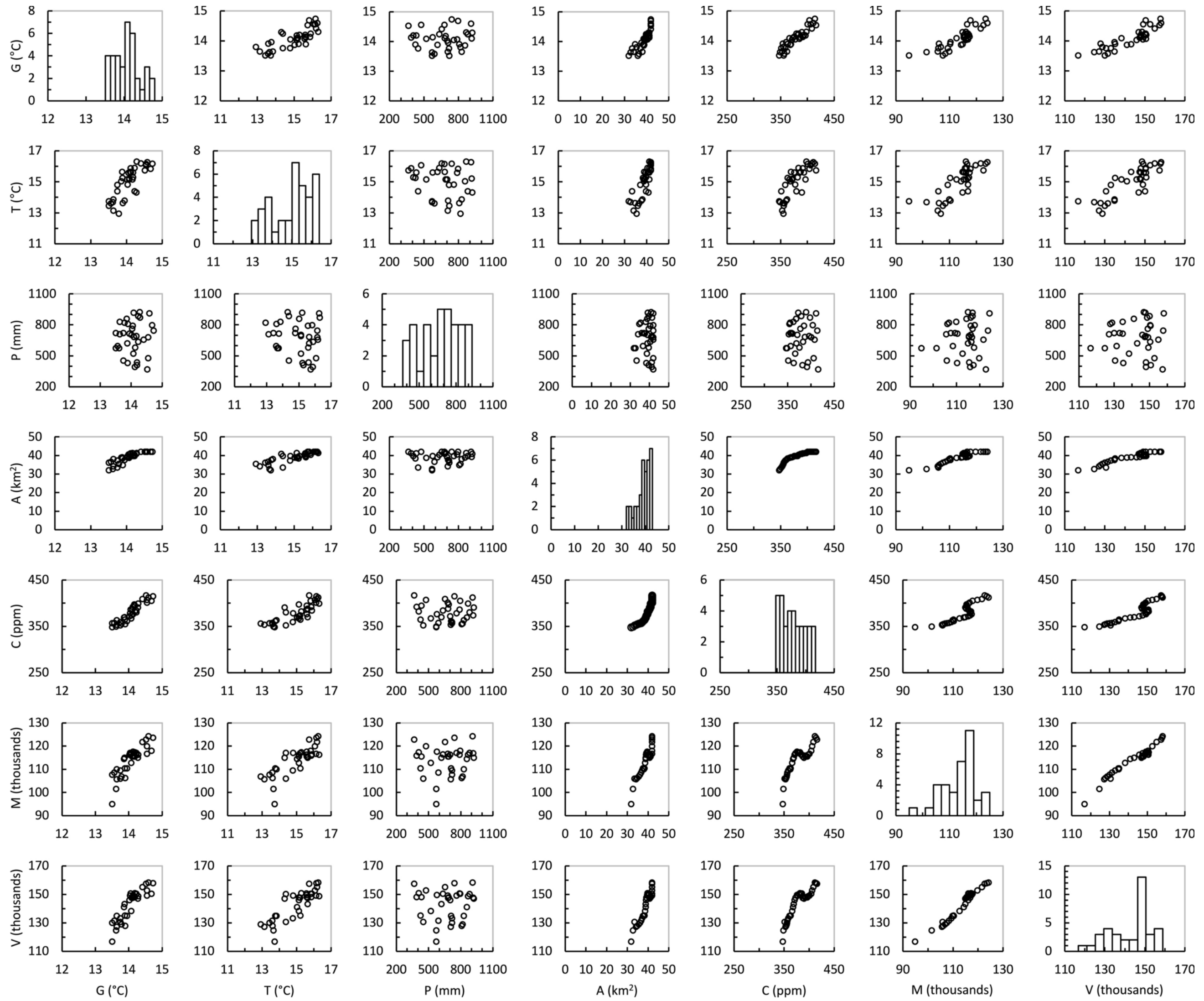

Fig. 4 Scatter plot matrix illustrating the absolute frequency distributions of *T, P, A, G, C, M*, and *V*, namely the number of occurrences *n* over discrete intervals observed over the period 1986–2021 and pairwise relationships

data values far from that point, as it does in other nonlinear regression methods such as polynomials (Perperoglou et al. 2019).

Let $\{x_i, y_i, i=1,\ldots, n\}$ be a set of observations modeled by the relation $y_i=f(x_i)+e_i$, where e_i are independent random variables. Let $\widehat{y}_i=f(x_i)$ denote the predicted values. Define a set of knots $\tau_1<\tau_2<\cdots<\tau_K$ within the range $[x_{\min}, x_{\max}]$, where $x_{\min}$ and $x_{\max}$ are the minimum and maximum values of x_i $(i=1,\ldots,n)$, respectively. A cubic spline function is a smooth function such that $f(x_i)$ is a polynomial of degree 3 and satisfies the property that all derivatives of order less than 3 are continuous. The flexibility of the function is determined by the number of knots. Increasing the number of knots results in more flexible curves. In the limiting case where each point x_i $(i=1,\ldots, n)$ is chosen as a knot, and each x_i corresponds to a unique value y_i, the spline perfectly interpolates the data. Assume that the function $f(x_i)$ is represented by a spline function with fixed knot sequence. Because the latter functions form a vector space, then it is possible to express $f(x_i)$ as

$$f\left(x_i\right) = \sum_{k=1}^{K+3+1} \beta_k B_k(x_i)$$

where B_k are a set of basis functions defining vector space and β_k are the associated spline coefficients. Representing $f(x_i)$ with basis functions shows that estimating $f(x_i)$ can be reduced to estimating the coefficients β_k for the transformed variables B_k. This estimation is a linear optimization problem and, more importantly, simplifies the spline modeling process to determining real-valued coefficients. In cubic splines, the basis functions are defined as follows:

$$B_1\left(x_i\right)=1, B_2\left(x_i\right)=x_i, B_3\left(x_i\right)=x_1^2, B_4=x_i^3.$$

Starting from the polynomial of degree 3 defined over [$x_{\min}$, $x_{\max}$], deviations from the base polynomial are successively added to the spline function to the right of each knot, such that:

$$B_4\left(x_i\right)=\left(x_i-\tau_1\right)^3+B_5\left(x_i-\tau_2\right)^3+\cdots+B_{K+4}\left(x_i-\tau_K\right)^3.$$

A notable feature of cubic splines is that their basis functions are not entirely local, as some are defined across the entire range of the data [$x_{\min}$, $x_{\max}$]. The spline has four parameters for each of the $K+1$ regions defined by the knots, minus three constraints per knot, resulting in $K+4$ degrees of freedom. The parameters are estimated using XLSTAT 2022 Statistical Software for Excel (Addinsoft 2023). This software performs cubic spline fitting with equally spaced knots but does not include a penalty function, such as the integrated second derivative of the spline. The primary tuning parameter in XLSTAT is the number of knots, which determines the smoothness of the fitted function. As Armstrong (2006) outlines, natural cubic splines are preferred for analyzing the relationship between temperature and other variables because they are constrained to be linear at the boundaries, where data are often too sparse to support more detailed modeling. Several authors emphasize that while spline modeling is highly flexible, it requires careful selection of tuning parameters (e.g., Friedman et al. 2001; Harrell 2015; Wood 2017). However, the degree of the polynomial (which can differ from 3 in other types of splines) and the spacing of the knots have been shown to have minimal impact on the fitting process. Cubic splines are generally preferred as they produce smooth curves. Polynomials of degree 1 or 2 often result in jagged splines, whereas polynomials of degree 3 and above yield curves with indistinguishable smoothness.

To avoid overfitting, the choice of a penalty function can be replaced by reducing the number of knots. Excessive knots introduce too many oscillations, while too few knots risk missing genuine variability in the data. In this study, the number of knots is selected by comparing the Akaike Information Criterion (AIC) and Bayesian Information Criterion (BIC). These criteria prevent overfitting by incorporating the model's degrees of freedom, unlike cross-validation strategies that optimize out-of-sample prediction. Since the objective of this study is not to maximize prediction accuracy but to determine which predictors provide the most explanatory power (potentially causal), AIC and BIC are particularly suitable. In terms of the sum of squared errors, BIC and AIC can be expressed as:

$$\mathrm{BIC}=n\,ln\sum_{i=1}^{n}\left(y_i-\widehat{y}_i\right)^2/n+kln(n)$$

and

$$\mathrm{AIC}=n\,ln\sum_{i=1}^{n}\left(y_i-\widehat{y}_i\right)^2/n+2k$$

where k is the number of parameters in the model. The penalty term k ln(n) in BIC is larger than the penalty term 2 k in AIC for $n>7$ (Stoica and Selen 2004).

Regression tree analysis is performed for multivariate regression, differing from many traditional flexible, non-parametric statistical techniques by providing insight into the role of each explanatory variable in predicting the dependent variable. Regression trees are well-suited for analyzing complex environmental data, offering robust and flexible methods capable of handling nonlinear relationships and high-order interactions. Despite the complexity of the algorithms used to construct these trees, the approach is intuitive and yields easily interpretable results. Regression trees explain variation in a single response variable by iteratively splitting the data into more homogeneous groups based on combinations of explanatory variables. Each group is characterized by the mean value of the response variable, the number of observations it contains, and the mean values of the explanatory variables defining it. Trees are often represented graphically, aiding in the interpretation of patterns and processes identified by the algorithms. Advantages of regression trees include their flexibility to handle various response types, invariance to monotonic transformations of explanatory variables, and ease of interpretation. Additionally, regression trees reveal the influence of explanatory variables on the dependent variable at different levels.

XLSTAT 2022 is used to fit regression trees, employing both the CHAID (Chi-squared Automatic Interaction Detection) and exhaustive CHAID algorithms, as well as the C&RT (Classification and Regression Tree) algorithm. CHAID builds upon the Automatic Interaction Detection (AID) algorithm developed by Morgan and Sonquist (1963), which performs stepwise splitting. AID begins with a single cluster of cases and searches for the best way to split the cluster into two, considering all possible splits for each predictor. The split that minimizes the within-cluster sum of squares about the cluster mean on the dependent variable is selected. AID also naturally incorporates interactions among predictors, represented in tree models by different branches from the same node, unlike the cross-product terms used in ANOVA models. CHAID extends the AID algorithm by incorporating adjusted significance testing (Kass 1980; Biggs et al. 1991; Ritschard 2013). For regression problems with continuous dependent variables, CHAID employs *F*-tests. Continuous predictors are first transformed into categorical variables by grouping their values into categories with approximately equal frequencies. The algorithm then identifies the least significant pair of predictor categories and merges them if their difference does not meet a predefined significance threshold (alpha-to-merge). This process is repeated until all remaining category pairs are significantly different. Bonferroni-adjusted *p*-values are computed to identify the most significant split. Splitting continues until no further splits meet the alpha-to-merge and alpha-to-split thresholds, resulting in terminal nodes. Tree size is controlled by parameters such as maximum tree depth and the alpha values for merging and splitting. Overly large trees can become difficult to interpret, so robustness to stopping rules and parameters should be evaluated to ensure meaningful and stable results. Furthermore, the appropriate tree size, balancing model complexity with interpretability, need to be selected.

Exhaustive CHAID, a modification of the basic CHAID algorithm, performs a more thorough merging and testing of predictor variables. Specifically, the merging of categories continues without reference to any alpha-to-merge value until only two categories remain for each predictor. The algorithm then follows the CHAID procedure for selecting the split variable, choosing the predictor that yields the most significant split. The parameters controlling the size of the tree are the maximum tree depth and the alpha-to-split value. C&RT (Breiman et al. 1984) is a similar algorithm designed for building binary trees. For all predictors, the algorithm computes the within-cluster sum of squares around the mean of the cluster for the dependent variable. The algorithm sorts all predictor values in ascending order, with each element of the sorted predictor serving as a potential splitting candidate or cut point. The optimal split is determined by maximizing the reduction in the within-cluster sum of squares across all candidates. Specifically, the algorithm splits the observations into two child nodes at each candidate, computes the reduction in the within-cluster sum of squares, and selects the candidate that yields the largest mean squared error (MSE) reduction. Tree building stops if the reduction in the within-cluster sum of squares is smaller than the specified complexity parameter (*cp*). In general, CHAID builds non-binary trees that tend to be wider, making this method particularly popular for certain applications. Conversely, C&RT always produces binary trees, which may sometimes be less efficient to summarize for interpretation. Regarding predictive accuracy, there are no universal recommendations in the literature, as the choice of algorithm remains an area of ongoing research. Both algorithms are applied and compared in this study to evaluate the robustness of results with respect to the chosen algorithm and splitting rules.

3 Results

3.1 Cubic splines

Table 1 presents the sum of squares errors (SSE), BIC, and AIC for cubic spline models predicting *T* as a function of *P*, *A*, and *C*, with varying numbers of knots ranging from 3 to 14. The BIC and AIC criteria are used to identify models with the optimal degree of smoothness, while SSE values are employed to compare model fit across different predictors. Both AIC and BIC favor the model with 4 knots when *P* is the predictor and the model with 5 knots when *A* or *C* is the predictor (the minimum value for each model selection criterion is highlighted in bold). The estimated fitting functions for these models are displayed in Fig. 5. The SSE values and fitted functions reveal that *A* and *C* provide very similar predictive information for *T*, whereas *P* is the weakest predictor. The high SSE and the overly smooth fitted function for *P*, where predicted values do not exceed 14 °C, suggest that *T* is unrelated to *P*. Fitted functions further demonstrate that *A* and *C* exhibit a monotonic direct relationship with *T* only above specific thresholds, approximately 20 km^2 for *A* and 325 ppm for *C*. The same analysis is conducted using D*T* as the dependent variable, and the results are presented in Table 2. As in the previous case, the models selected by the information criteria are the cubic spline with four knots

Table 1 Sum of squares errors (SSE), BIC, and AIC for cubic spline models with varying numbers of knots, modeling T as a function of P, A, and C for the period 1881–2021. The minimum values for each model selection criterion are highlighted in bold

# of knots	*P*			*A*			*C*		
	SSE	BIC	AIC	SSE	BIC	AIC	SSE	BIC	AIC
3	267.0	822.5	801.8	259.5	818.5	797.8	169.0	758.0	737.3
4	**158.7**	**754.0**	**730.4**	344.6	854.9	831.3	88.5	671.7	648.1
5	238.9	816.7	790.2	**64.7**	**632.6**	**606.1**	**65.7**	**634.7**	**608.1**
6	194.4	792.5	763.1	87.3	679.8	650.3	96.7	694.2	664.7
8	141.1	757.2	721.8	103.8	714.0	678.6	92.9	698.4	663.1
10	178.5	800.3	759.1	119.2	743.4	702.2	75.7	678.9	637.6
12	462.5	944.5	897.3	191.4	820.1	772.9	66.2	670.3	623.1
14	220.7	850.0	797.0	129.1	774.4	721.4	76.1	699.9	646.8

Fig. 5 Fitted cubic spline functions modelling *T* as a function of *P* (left), *A* (center), and *C* (right) for the period 1881–2021

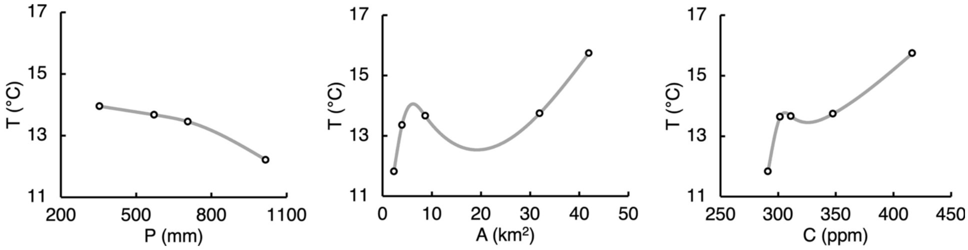

Table 2 Sum of squares error (SSE), BIC, and AIC for cubic splines with different number of knots modelling DT as a function of P, A, and C for the period 1881–2021. The minimum values for each model selection criterion are highlighted in bold

# of knots	*P*			*A*			*C*		
	SSE	BIC	AIC	SSE	BIC	AIC	SSE	BIC	AIC
3	168.9	757.9	737.3	195.8	778.7	758.1	157.3	747.8	727.2
4	**72.5**	**643.5**	**619.9**	334.4	859.1	835.5	100.9	690.2	666.6
5	147.6	748.8	722.2	**62.4**	**627.4**	**600.9**	**66.7**	**636.7**	**610.2**
6	87.5	679.9	650.5	71.8	652.2	622.7	80.2	667.8	638.3

Fig. 6 Fitted cubic spline functions modelling D*T* as a function of *P* (left), *A* (center), and *C* (right) for the period 1881–2021

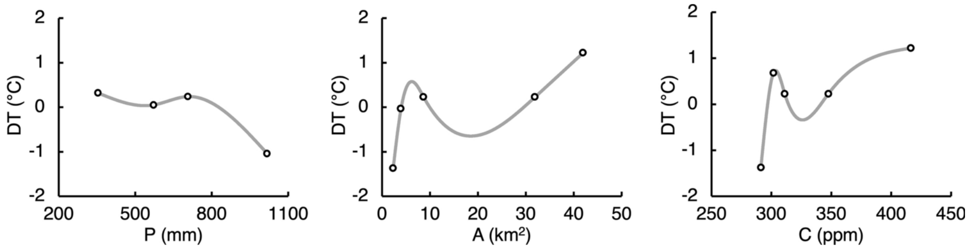

when *P* is used as a predictor and the cubic spline with five knots when *A* or *C* are used as predictors. SSE, BIC, and AIC values for models with more than six knots are higher and, therefore, are not reported in Table 2. Estimated fitting functions for the selected models are shown in Fig. 6. SSE results indicate that *A* and *C* have the greatest impact on the dependent variable D*T*, with *P* having a slightly lesser effect. The fitted functions reveal that D*T* is inversely related to *P*, while *A* and *C* exhibit a monotonic direct relationship with D*T* only for values exceeding the same thresholds previously identified (approximately 20 km^2 for *A* and 325 ppm for *C*).

Tables 3 and 4 report the sum of squared errors (SSE), BIC, and AIC for cubic splines with different numbers of knots, modeling *T* and D*T*, respectively, as functions of *P*, *A*, *C*, the number of cars (*M*), and vehicles (*V*) for the second data set of 36 annual observations from 1986 to 2021. For both predicting *T* and D*T*, AIC and BIC favor the model with three knots when using *P*, *A*, *C*, or *V* as the independent variable, and the model with four knots when using *M* as the independent variable. SSE comparison indicates that *P* is the worst predictor for *T* and D*T*, while *A*, *C*, *M*, and *V* convey similar information in predicting *T* and D*T*. The selected fitted functions are graphically displayed in Figs. 7 and 8. The shape of these functions suggests that, since 1986, *A*, *C*, and *V* have a monotonic direct relationship with *T* and D*T*, indicating that we may expect further increases in both *T* and D*T* as these variables increase. In contrast, the relationship between *T* and D*T* and cars is not monotonic, showing a change in direction after a certain threshold. This suggests that further increases in the number of cars may not result in additional increases in *T* and D*T*. As expected, *P* is inversely related to both *T* and D*T*. By analyzing the shape of the fitted functions one can expect higher values of *T* and D*T* for larger values of *P*. In summary, cubic spline analysis shows that, when used separately, variables explaining local development, such as *A*, cars, and *V*, are similarly strong predictors of local temperature and the difference between local and global temperature, compared to the global development variable *C*. These local variables are thus effective surrogates for the global development variable *C* in the urban city of Modena. The local climatic variable *P* cannot be considered a good predictor of *T*, but it may be useful in predicting the difference D*T*.

3.2 Regression trees

The CHAID and exhaustive CHAID regression trees modeling *T* as a function of *P*, *A*, and *C* for the period 1881–2021 yield nearly identical results. Without imposing restrictions on the maximum tree depth, the resulting trees consist of only one level. The selected split variable is *A*. The choice of alpha parameters affects only the number of nodes in the first level. Figure 9 shows the regression tree obtained

Table 3 Sum of squares error (SSE), BIC, and AIC for cubic splines with different number of knots modelling T as a function of P, A, C, M, and V for the period 1986–2021. The minimum values for each model selection criterion are highlighted in bold

# of knots	*P*			*A*			*C*			*M*			*V*		
	SSE	BIC	AIC	SSE	BIC	AIC	SSE	BIC	AIC	SSE	BIC	AIC	SSE	BIC	AIC
3	**38.6**	**156.6**	**145.5**	**11.6**	**113.3**	**102.2**	**13.7**	**119.4**	**108.4**	22.9	137.7	126.7	**11.5**	**112.9**	**101.8**
4	43.0	164.1	151.4	47.3	167.5	154.8	31.8	153.2	140.5	**18.0**	**132.7**	**120.1**	21.1	138.4	125.8
5	51.3	174.0	159.8	13.5	125.9	111.7	17.1	134.5	120.2	38.6	163.7	149.5	14.6	128.7	114.5

using both CHAID and exhaustive CHAID algorithms with all alpha parameters set to 5%, while Table 5 illustrates the tree structure. The target variable in the root node is *T*, and the first (and only) split variable is *A*. Table 5 lists the rules derived from both the CHAID and exhaustive CHAID models, following the nodes and branches. These rules are based on a single level of the tree, with all three rules involving the variable *A*, indicating that it is the only predictor selected by both algorithms. Understanding the rules makes the model more interpretable. For example, Rule 1 indicates that if *A* in a given year is lower than 16.21 km^2, the expected average annual temperature is 13.2 °C. Rule 2 suggests that if *A* is between 16.21 and 36.6 km^2, the expected annual average urban temperature is 13.52 °C. Rule 3 states that if *A* exceeds 36.6 km^2, the expected average annual temperature is 13.38 °C. All these rules are end nodes, representing the outcomes of decision paths. This interpretative logic can be applied to all subsequent trees.

In Fig. 10, the regression tree obtained using the C&RT algorithm with a complexity parameter (*cp*) of 0.01 is shown, and Table 6 displays the tree structure. In this tree, the first-level predictor is *C*, with *A* appearing as a second-level predictor only for values of *C* below 363.31 ppm. When the complexity parameter *cp* ranges from 0.05 to 0.01, the tree structure remains unchanged. However, with a very small *cp* set to 0.001, the tree becomes overly complex, with many layers and nodes in each layer, making it difficult to interpret. The importance of each feature in the regression tree model can be assessed by analyzing the levels. According to the CHAID and exhaustive CHAID algorithms, *A* is the most important predictor of *T*. In contrast, the C&RT algorithm identifies *C* as the most important predictor, with *A* playing a secondary role. For all algorithms, *P* is the least important feature among the considered variables, having the smallest effect on *T*. *P* is not selected as a split variable when changing the CHAID and exhaustive CHAID stopping parameters, while it appears as the third-level predictor in C&RT with a complexity parameter $cp = 0.001$.

Figure 11 reports the regression tree modeling D*T* as a function of *P*, *A*, and *C* for the period 1881–2021, obtained using the CHAID and exhaustive CHAID algorithms with alpha values ranging from 0.1 to 0.01. The results are stable with respect to both the algorithm used and the stopping parameters, and they indicate that *A* is the only variable important for predicting the difference between the local urban temperature and the global temperature. For *A* values lower than 36.6 km^2, the expected difference is zero, indicating that positive and negative differences balance each other out when urbanization is below this threshold. For $A > 36.6$ km^2, the expected difference is positive, suggesting that the local urban temperature is expected to be higher than the global one when local urbanization exceeds this threshold.

Table 4 Sum of squares error (SSE), BIC, and AIC for cubic splines with different number of knots modelling DT as a function of P, A, C, M and V for the period 1986–2021. The minimum values for each model selection criterion are highlighted in bold

# of knots	*P*			*A*			*C*			*M*			*V*		
	SSE	BIC	AIC	SSE	BIC	AIC	SSE	BIC	AIC	SSE	BIC	AIC	SSE	BIC	AIC
3	**23.2**	**138.3**	**127.2**	**12.1**	**114.7**	**103.6**	**13.1**	**117.8**	**106.7**	18.5	130.1	119.0	**11.1**	**111.8**	**100.8**
4	29.3	150.3	137.7	45.1	165.8	153.1	31.4	152.7	140.0	**12.6**	**120.0**	**107.3**	14.2	124.2	111.5
5	32.3	157.3	143.1	14.1	127.5	113.2	16.6	133.4	119.2	31.6	156.6	142.4	15.4	130.7	116.4

Figure 12 reports the regression tree modeling D*T* as a function of *P*, *A*, and *C* for the period 1881–2021, obtained using C&RT with a $cp = 0.01$. Table 7 presents the tree structure.

For *cp* values higher than 0.01, the regression trees have only the first level, with *A* selected as the split variable (and a threshold value of 38.15 km^2). For *cp* values smaller than 0.01, the trees have a third level with *A* as the split variable again, and a fourth level with *P* as the split variable. The results indicate that *A* is the most important variable for predicting D*T*, and *P* is only important for predicting D*T* when local urbanization is lower than 38.15 km^2. For $A \leq 38.15$ km^2 and $P \leq 962.95$ mm, the expected local urban temperature is nearly equal to the global one. However, for $P > 962.95$ mm, the expected local urban temperature is higher than the global one. For $A > 38.15$ km^2, the expected local temperature is higher than the global one, and *P* does not influence the difference between *G* and *T*.

When using the second dataset to model *T* as a function of *P*, *A*, *C*, *M*, and *V* for the period 1986–2021, trees obtained with the CHAID and exhaustive CHAID algorithms have only one level: the variable selected as the split variable is either A or C, depending on the alpha values. Figure 13 shows the regression tree obtained with CHAID (with α, alpha-to-merge, and alpha-to-split set to 0.01) and exhaustive CHAID (with α set to 0.01). Figure 14 presents the regression tree obtained with CHAID (with α, alpha-to-merge, and alpha-to-split set to 0.5) and exhaustive CHAID (with α set to 0.5). The results indicate that, from 1986 onward, *A* and *C* are similarly strong predictors of *T*. The C&RT algorithm, with *cp* set to 0.01, on the other hand, selects *V* in the first level and *C* in the second level. With a very small *cp* value set to 0.001, the tree has a third level in which the split variable selected is *P*. Figure 15 shows the regression tree with *cp* set to 0.01. With the C&RT algorithm, regression trees indicate that *V* is the most important variable for predicting *T*, and *C* is important only when the number of vehicles exceeds 135,039.

Comparing Figs. 13, 14, and 15, it can be observed that an average urban air temperature of 13.72 °C is achieved with either $A \leq 37.98$ km^2 or $V \leq 135{,}039$, while a slightly lower average temperature of 13.56 °C corresponds to $C \leq 356.54$ ppm. An average temperature of 15.2 °C is reached with either $37.98 < A \leq 40.80$ km^2 or $V > 135{,}039$, combined with $C \leq 397.81$ ppm. An intermediate range of 14.49 °C to 15.6 °C occurs when $356.54 < C \leq 398.87$ ppm. The highest average urban air temperature, near 16 °C, is observed with $A > 40.8$ km^2, $V > 135{,}039$, or $C > 397.81$ ppm, as well as when $C > 398.87$ ppm. These results indicate that *A* and *C* are similarly strong predictors of urban air temperature, with *V* also emerging as a strong predictor when used in conjunction with *C*.

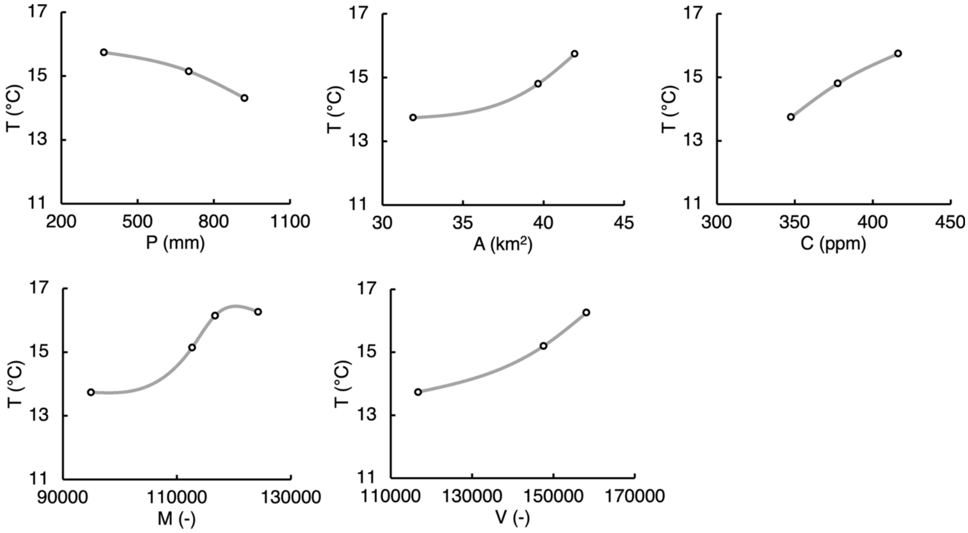

Fig. 7 Fitted cubic spline functions modelling *T* as a function of *P* (top left), *A* (top center), *C* (top right), *M* (bottom left), and *V* (bottom center) for the period 1986–2021

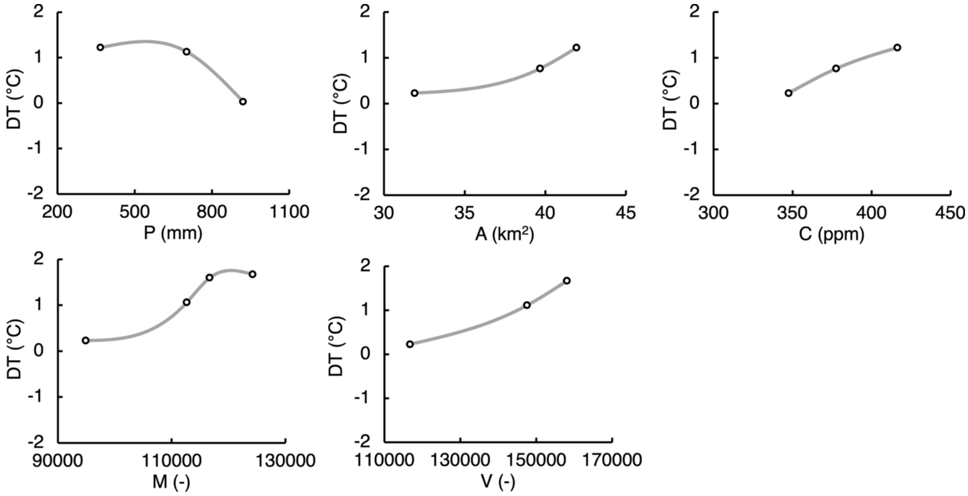

Fig. 8 Fitted cubic spline functions modelling D*T* as a function of *P* (top left), *A* (top center), *C* (top right), M (bottom left), and *V* (bottom center) for the period 1986–2021

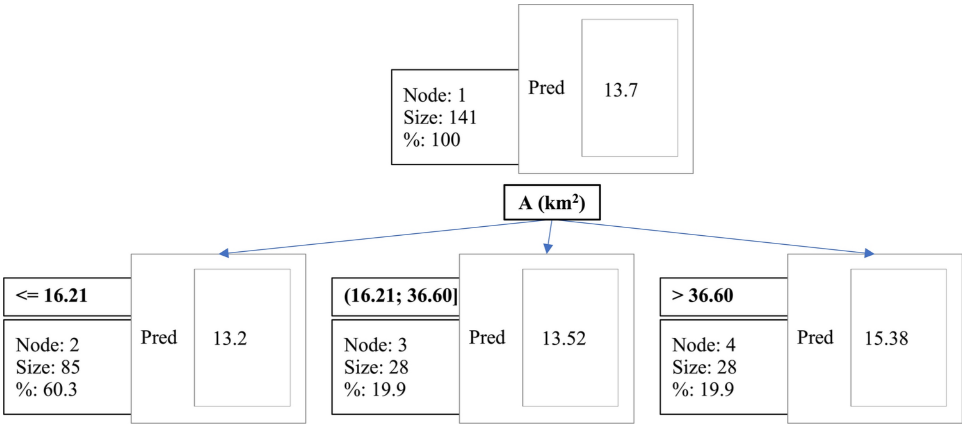

Fig. 9 CHAID (with α set to 5%, alpha-to-merge and alpha-to-split values set to 5%) and exhaustive CHAID (with α set to 5%) regression trees modeling *T* as a function of *P*, *A*, and *C* for the period 1881–2021

Table 5 Structure of CHAID (with α set to 5%, alpha-to-merge and alpha-to-split values equal to 5%) and exhaustive CHAID (with α set to 5%) trees modeling T as a function of P, A, and C for the period 1881–2021

Node	# of years	%	Test statistic	*p*-value	df1	df2	Split variable	Values
1	141	100.00	176.14	<0.0001	2	138		
2	85	60.28					A (km^2)	≤ 16.21
3	28	19.86					A (km^2)	(16.21, 36.60]
4	28	19.86					A (km^2)	>36.60

Fig. 10 C&RT regression tree with *cp* set to 0.01 modeling *T* as a function of *P*, *A*, and *C* for the period 1881–2021

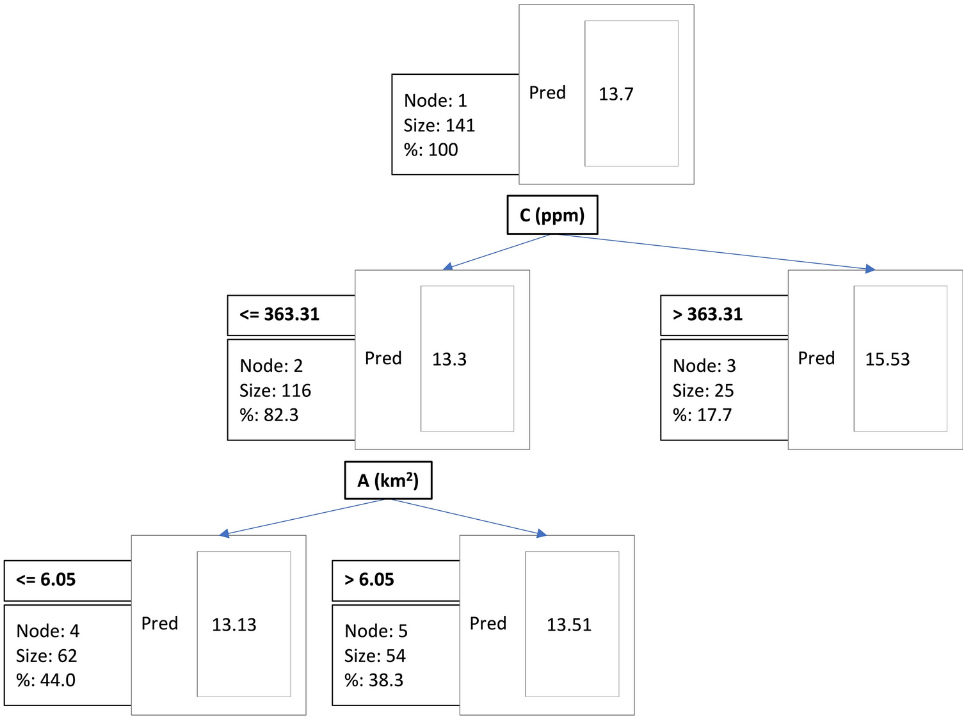

Table 6 Structure of the C&RT tree (with *cp* set to 0.01) modeling *T* as a function of *P*, *A*, and *C* for the period 1881–2021

Node	# of years	Coverage (%)	Improvement	Split variable	Values	Parent node	Sons	Predicted values
1	141	100	0.725				2; 3	13.7
2	116	82.27	0.130	*C* (ppm)	≤363.31	1	4; 5	13.3
3	25	17.73		*C* (ppm)	>363.31	1		15.53
4	62	43.97		*A* (km^2)	≤6.05	2		13.13
5	54	38.30		*A* (km^2)	>6.05	2		13.51

Fig. 11 CHAID (with α, alpha-to-merge, and alpha-to-split values ranging from 0.01 to 0.1) and exhaustive CHAID regression tree (with α ranging from 0.01 to 0.1) modeling D*T* as a function of *P*, *A*, and *C* for the period 1881–2021

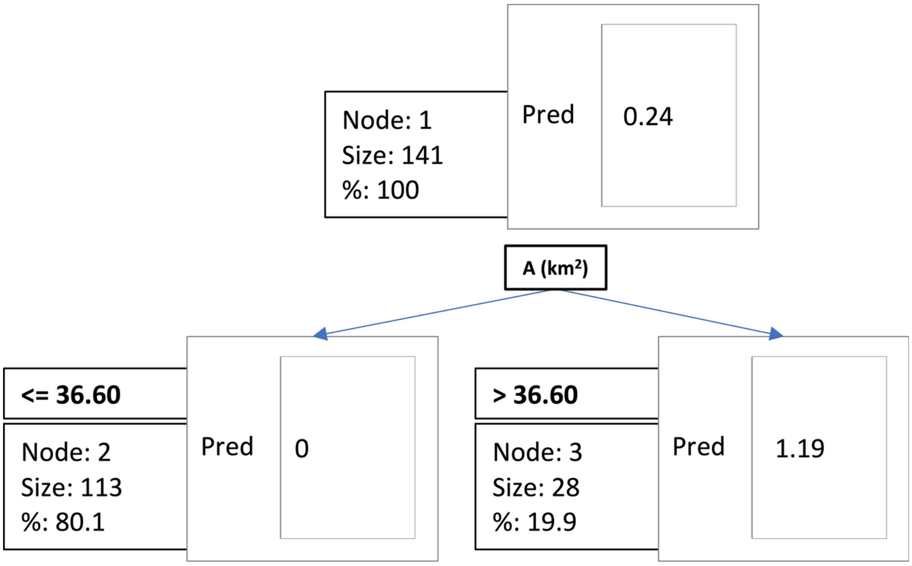

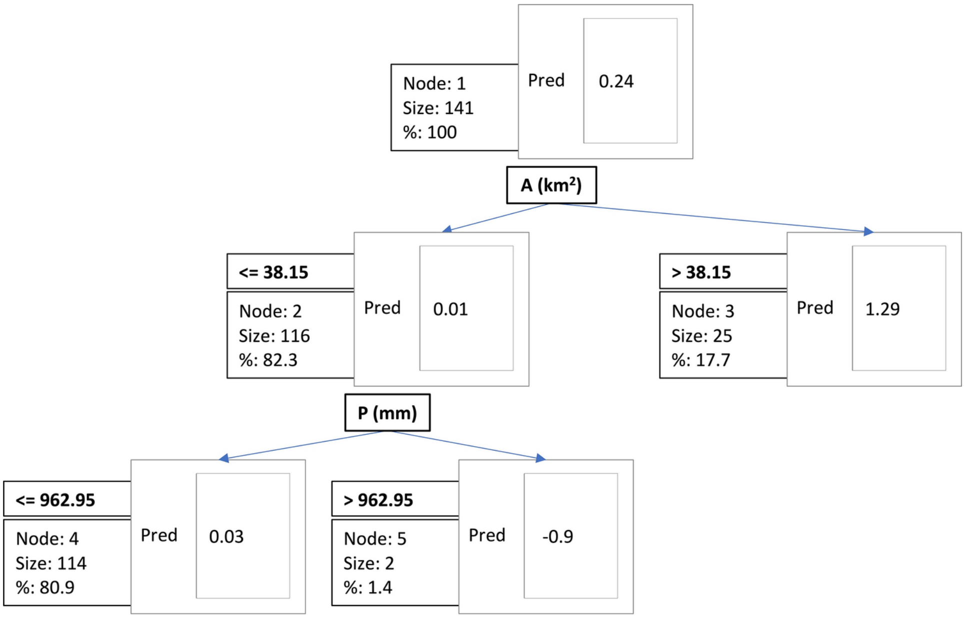

Fig. 12 C&RT (with *cp* set to 0.01) modeling DT as a function of P, A, and C for the period 1881–2021

Table 7 Structure of the C&RT tree (with *cp* set to 0.01) modelling DT as a function of P, A, and C for the period 1881–2021

Node	# of years	Coverage (%)	Improvement	Split variable	Values	Parent node	Sons	Predicted values
1	141	100.00	0.494				2; 3	0.24
2	116	82.27	0.060	A (km^2)	≤38.15	1	4; 5	0.01
3	25	17.73		A (km^2)	>38.15	1		1.29
4	114	80.85	0.037	P (mm)	≤962.95	2		0.03

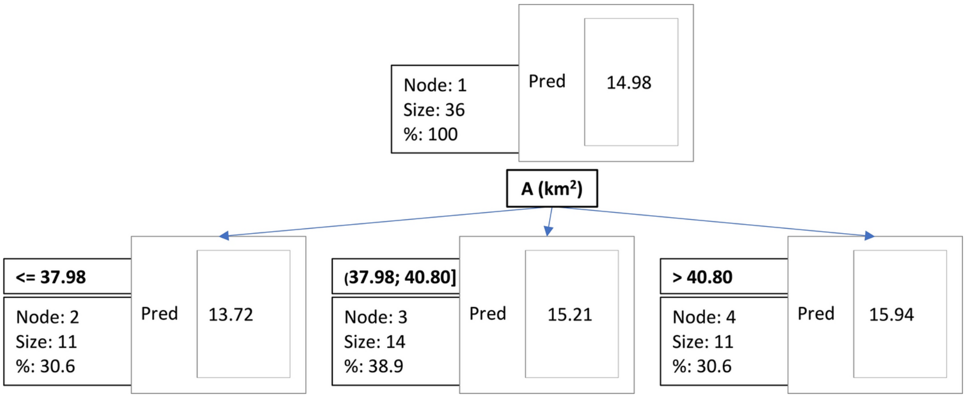

Fig. 13 CHAID (with α, alpha-to-merge, and alpha-to-split set to 0.01) and exhaustive CHAID regression tree (with α set to 0.01) modelling T as a function of P. A, C, M and V for the period 1986–2021

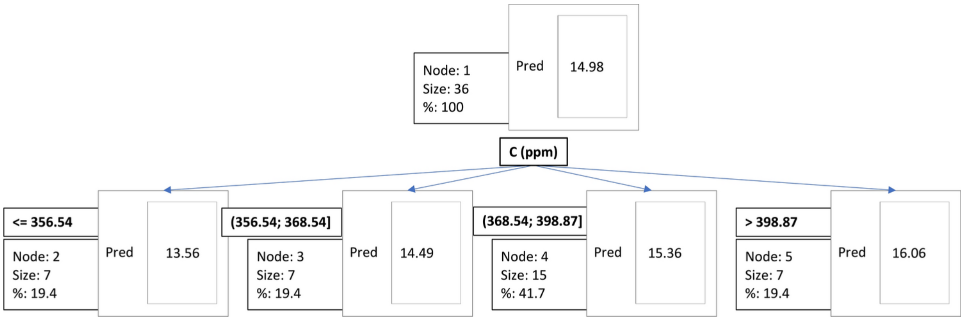

Fig. 14 CHAID (with α, alpha-to-merge, and alpha-to-split set to 0.05) and exhaustive CHAID regression tree (with α set to 0.05) modeling T as a function of P, A, C, M, and V for the period 1986–2021

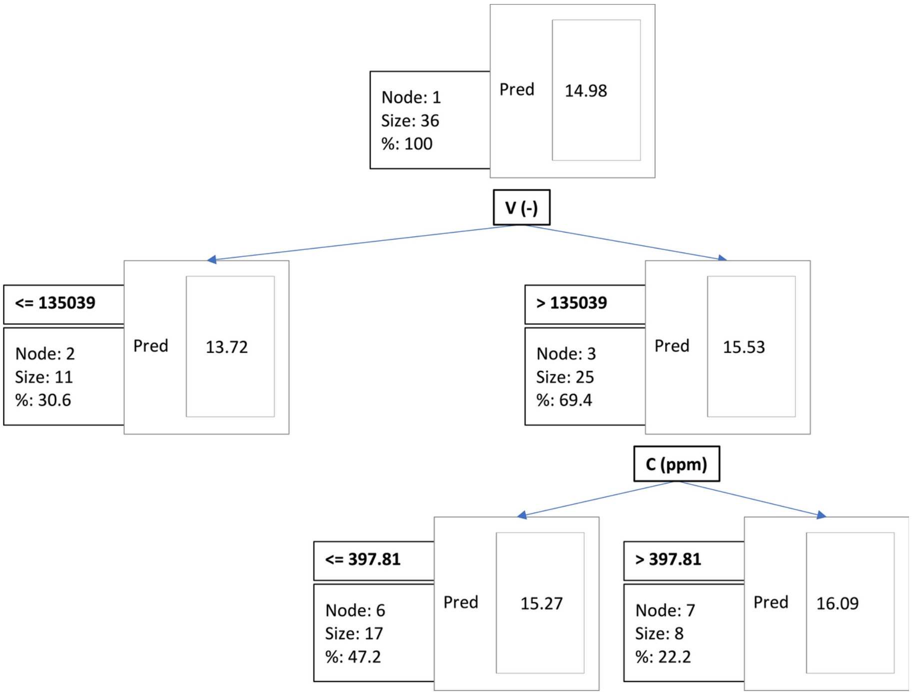

Fig. 15 C&RT (with cp set to 0.01) modeling T as a function of P, A, C, M and V for the period 1986–2021

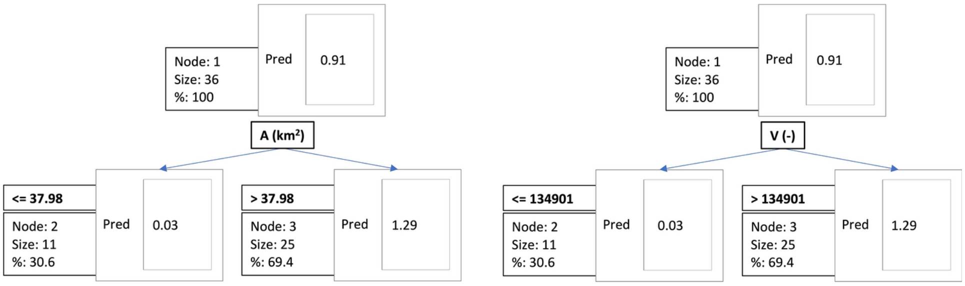

Fig. 16 CHAID (with α, alpha-to-merge and alpha-to-split set to 0.01) and exhaustive CHAID regression tree (with α set to 0.01) modeling DT as a function of P, A, C, M and V for the period 1986–2021 (left panel) and CHAID (with α, alpha-to-merge, and alpha-to-split set to 0.05) and exhaustive CHAID regression tree (with α set to 0.05) modeling DT as a function of P, A, C, M, and V for the same period (right panel)

When using the second data set to model DT as a function of P, A, C, M, and V (for the period 1986–2021), the CHAID and exhaustive CHAID algorithms select either A or V, depending on the α values. With CHAID, when α, alpha-to-merge, and alpha-to-split are set between 0.05 and 0.1, the selected variable is V. Conversely, when α, alpha-to-merge, and alpha-to-split are set between 0.01 and 0.04, the selected variable is A. Exhaustive CHAID yields similar results. Figure 16 presents the trees obtained with CHAID (α, alpha-to-merge, and alpha-to-split set to 0.01) and exhaustive CHAID (α set to 0.01) on the left, and CHAID (α, alpha-to-merge, and alpha-to-split set to 0.05) and exhaustive CHAID (α set to 0.05) on the right. The results indicate that A and V provide equivalent information for predicting DT. A local urban air temperature nearly equal to the global temperature is expected when either $A \leq 37.98$ km^2 or $V \leq 134{,}901$. Conversely, a local urban air temperature higher than the global one is expected when $A > 37.98$ km^2 or $V > 134{,}901$. The C&RT algorithm selects A at the first level and P at the second level when $cp \leq 0.01$. Figure 17 shows the tree obtained with cp values ranging from 0.001 to 0.01.

Results indicate that, from 1986 onward, both the local urban air temperature and the difference between this local temperature and the global one can be predicted using only A, C, or V. The local variables A and V provide similar information to C in explaining local temperature. In contrast, the local climatic variable P is useful only when combined with A or C. These findings suggest that local policies aimed at limiting urbanization, reducing the number of vehicles, and curbing local development can effectively help mitigate increases in local urban air temperature. Regression tree analysis further demonstrates that, when used individually, A, C, and V (the latter applicable only from 1986) are

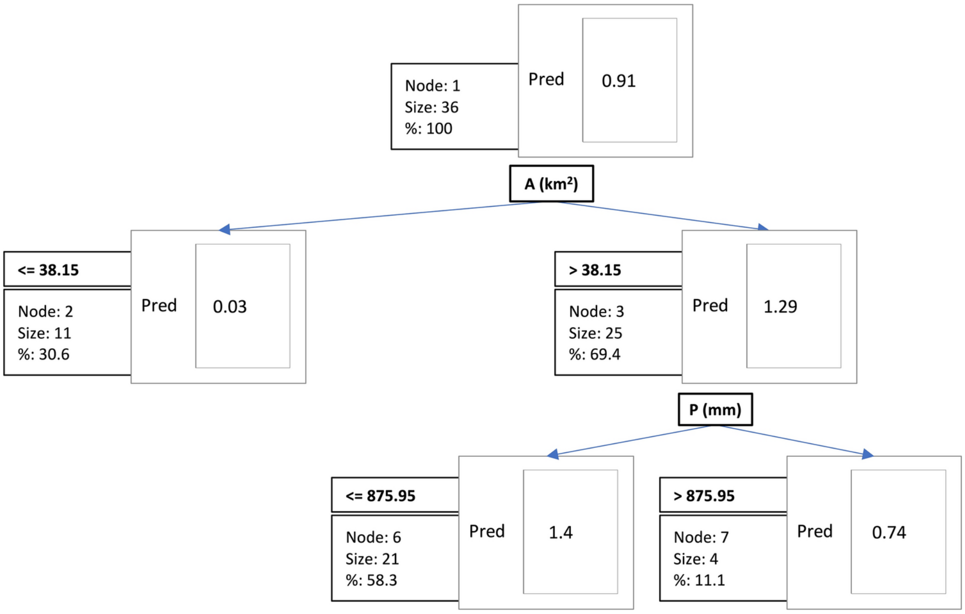

Fig. 17 C&RT (with *cp* ranging from 0.001 to 0.01) modeling D*T* as a function of *P*, *A*, *C*, *M*, and *V* for the period 1986–2021

similarly strong predictors of *T* and perform nearly as well as when used together. Thus, *A* and *V* (from 1986 onward) serve as effective surrogates for *C* in predicting local urban air temperature, whereas *P* is significant for explaining D*T* only when paired with another variable representing local or global development.

3.3 Order of magnitude analysis

An order-of-magnitude analysis using reasonable scale variables is performed to test the plausibility of the hypothesis that the rapid increase in local temperature relative to global temperature observed in Modena since 1996 is caused, at least in part, by congested traffic heating. The local temperature increase, δT, relative to global temperature is given by

$$\delta T = Q/C_p,$$

where Q is the heat released by traffic to the near-surface atmospheric layer involved in J, and C_p is the heat capacity of this atmospheric layer in J K^{-1}. C_p represents the amount of heat required to produce a unit change in the temperature of the atmospheric layer, and can be expressed as

$$C_p = c_p M_a,$$

where c_p is the air specific heat capacity in J kg^{-1} K^{-1} and M_a is the mass of air involved in kg. M_a can be computed as

$$M_a = \rho_a A\ Z,$$

where ρ_a is the air density in kg m^{-3}, A is the urban area extent in m^2, and Z is the thickness of the atmospheric urban roughness sublayer in meters, which can conservatively be set to six times the average building height in the city. In the case of Modena, assuming $\rho_a = 1.225$ kg m^{-3}, $A = 42 \times 10^6$ m^2, $Z = 60$ m, and $c_p = 1006$ J kg^{-1} K^{-1}, it follows that $M_a = 3.087 \times 10^9$ kg, and $C_p = 3.106 \times 10^{12}$ J K^{-1}.

The traffic heat release, Q, to the near-surface atmospheric layer involved is given by

$$Q = H\ F,$$

where H is the heat value of gasoline or diesel fuel in J kg^{-1} and F is the daily fuel consumption in kg. F can be estimated as

$$F = f\ V_i,$$

where f is the average daily fuel consumption of a vehicle circulating within the considered municipal district, and V_i is the number of vehicles involved. For Modena, assuming $f = 3$ kg/vehicle, $V_i = 78{,}130$ vehicles (half the average number of registered vehicles in the municipal district in the five years from 2017 to 2021), and $H = 46 \times 10^6$ J kg^{-1}, it follows that $F = 234{,}390$ kg and $Q = 1.078 \times 10^{13}$ J. It is finally obtained that $\delta T = 3.5$ K, or equivalently $\delta T = 3.5$ °C, which is of the same order of magnitude as the local temperature excess observed in Modena since 1996 (Figs. 1 and 6).

4 Discussion

The GISTEMP series provides global surface temperature anomalies relative to the 1951–1980 baseline. In this study, absolute temperatures for Modena are estimated by adding

GISTEMP anomalies to the local mean temperature for that period, using data from the Osservatorio Geofisico di Modena. This standard approach assumes temperature stability during the baseline and is supported by the close match between observed and reconstructed values for 1951–1980. Adding GISTEMP anomalies to the local mean anchors global data to an absolute temperature scale, a widely accepted practice in climatology. However, applying global anomalies to specific locations assumes uniform warming rates, an assumption that may not always hold. Ideally, grid-point anomalies (e.g., the $1° \times 1°$ cell containing Modena) could be used instead. A comparison of global, gridded, and local data is presented in Appendix 3. Nevertheless, because the study focuses on local deviations from the global mean, the global GISTEMP series is preferred over gridded data, which inherently include local effects. This approach highlights the significance of local temperature trends in relation to global patterns. A statistical analysis is conducted to assess how local temperatures have deviated from the global mean over the past two decades. The alignment of local and global temperatures during the 1951–1980 baseline, followed by divergence after 1990, is a central focus of this study. The statistical findings support those of Morlini et al. (2024), which identified relationships between local temperature (*T*) in Modena and factors such as urbanization (*A*), precipitation (*P*), and global CO_2 levels (*C*). This research extends that analysis by examining deviations of local temperatures from global averages and by incorporating additional variables, specifically the number of cars (*M*) and vehicles (*V*), to account for anthropogenic heat effects. In doing so, it deepens the understanding of how global and local factors interact to influence urban air temperature. New statistical methods are used to explore these relationships, including splines and regression trees. Regression trees are also employed to identify change points in the dependencies among the multivariate series.

Spline analysis indicates that *A* (local urbanization) and *C* (global CO_2 concentration) provide very similar information in predicting *T* (local temperature) and reveals that *P* (precipitation) is a poor predictor when considered alone (Table 1 and Fig. 5). It also shows that *A* and *C* have a strong, monotonic direct relationship with *T* for values above a certain threshold, approximately 20 km^2 for *A* and 325 ppm for *C*. Notably, these threshold values have occurred since 1970 for both *A* and *C*. These findings align with those of Morlini et al. (2024), which used Buishand's test analysis to identify 1970 and 1965 as change points for the *C* and *A* series, respectively (Buishand 1982, 1984). The new insight provided in the present study is that the shifts in the mean of these series mark the onset of the strong direct relationship between increases in *A* and *C* and the rise in *T*. When analyzing the difference D*T* ($DT=T-G$) as the dependent variable, splines reveal that *P* can be a useful predictor, along with *A* and *C* (Table 2 and Fig. 6). *P* values exceeding 700 mm are associated with significant negative deviations in local temperature relative to global temperature, likely due to enhanced evaporative cooling in the local environment. Conversely, *A* values above 35 km^2 and *C* values exceeding 350 ppm led to notable positive deviations, suggesting that unsustainable global and local development negatively affect the local ecosystem.

Over the past 35 years, during which data on the number of registered cars (*M*) and vehicles (*V*) in Modena have been available, spline analysis reveals that local variables related to anthropogenic urban heat– such as urban area extent (*A*), the number of cars (*M*) and vehicles (*V*), and global CO_2 concentration (*C*)– have similar predictive power for local temperature (*T*) and the deviation (D*T*) of local temperature (*T*) from global temperature (*G*) (Tables 3 and 4). The fitted functions suggest that increases in the number of vehicles exert the most significant impact on both local temperature and its deviation from the global average (Figs. 7 and 8). Although further research is required for reliable validation, an order-of-magnitude analysis supports the plausibility of this hypothesis (Sect. 3.3). Even if it is assumed that not all of the traffic heat release *Q* contributes to the temperature increase δT, but is instead partially stored or released outside the atmospheric urban roughness sublayer, the order of magnitude of δT would still be comparable to the local deviations observed in Modena. The order-of-magnitude analysis in this section indicates that traffic-induced anthropogenic heat can be a significant contributor, particularly when the number of vehicles exceeds the transport system's capacity, leading to congestion. Complex geometries that trap incoming radiation are also known to influence the urban climate. However, the heat released by traffic, *Q*, may be an additional internal source that is transferred to the atmosphere either directly or indirectly after warming objects in the urban area. The order-of-magnitude analysis serves to verify the physical plausibility of the statistical conclusions within the constraints of an annual heat balance. Daily effects cannot be accurately captured by annual variables.

A visual analysis of monthly local temperatures indicates that similar patterns persist across all months of the year (Appendix 1, Fig. 18). This observation suggests that anthropogenic heat effects that remain relatively constant throughout the year (e.g., those associated with vehicle use) play a more significant role compared to anthropogenic heat effects that exhibit seasonality (e.g., winter heating and summer air conditioning). An attempt was made to identify the possible impact of the COVID-19 pandemic in spring 2020 in Italy on monthly temperatures for March and May 2020, during which a lockdown was imposed, significantly affecting traffic. The difference in monthly temperatures between the city of Modena and the surrounding stations of Albareto, Castelfranco Emilia, Formigine, and Marzaglia shows a temperature variation of about 2 °C throughout the year, which was not significantly affected by COVID-19-related traffic restrictions. However, it is possible that these restrictions had a similar impact on temperature measurements in both Modena and the surrounding stations, as traffic congestion could also occur near the stations in Albareto, Castelfranco Emilia, Formigine, and Marzaglia. In any case, the impact of the COVID-19 pandemic on the presented analysis of annual data may have been limited or difficult to discern, as traffic restrictions lasted only a few months.

Multivariate analysis using regression trees confirms the findings of Morlini et al. (2014) obtained with general additive models: the local variable P is useful for predicting local temperature only when combined with a global or local variable related to development. According to CHAID and exhaustive CHAID algorithms, A (urban area extent) is the most important feature for predicting T (local temperature), whereas C&RT identifies C (CO_2 concentration) as the most significant feature, with A playing a secondary role (Figs. 9 and 10, Tables 5 and 6). Notably, A provides the best predictions when used alone, while C requires interaction with A to achieve optimal predictions of T. When $A \leq 16.2$ km^2, the expected annual mean local temperature is 13.2 °C. For A between 16.21 and 36.6 km^2, the mean temperature rises to 13.52 °C, an increase of 0.32 °C. For $A \geq 36.6$ km^2, the mean temperature further increases to 15.38 °C, representing an additional rise of 1.86 °C (Fig. 9; Table 5). Regression trees, which model asymmetric nonlinear relationships, suggest that the increase in urban area extent is a primary driver of local temperature rise. It is worth noting that $A \leq 16.2$ km^2 corresponds to years before 1965, A between 16.21 and 36.6 km^2 corresponds to 1965–1993, and $A \geq 36.6$ km^2 corresponds to years after 1993. The years 1965 and 1993 were identified as change points for the T series using the Pettitt and Buishand tests, respectively (Morlini et al. 2014). In this work, these change points are detected through multivariate analysis and mark shifts in the relationship between T and other variables. When C is selected as the best predictor (Fig. 10; Table 6), a change from $C \leq 363.31$ ppm to higher values leads to an increase in the average temperature of 2.23 °C, from 13.3 °C to 15.53 °C. This change in the CO_2 series occurs in 1996, identified as a change point in temperature using the SNHT test (Morlini et al. 2014). In summary, C is the best predictor of changes in local temperature before and after 1996, while A serves as the best predictor for local changes during the periods 1881–1965, 1966–1993, and 1994–2021. When considering the deviation of local temperature from global temperature as the dependent variable, all algorithms select A as the best predictor, either in combination with P (Fig. 12; Table 7) or singly (Fig. 11). Positive average predicted deviations are associated with $A > 36.6$ km^2 (after 1993) and $A > 38.15$ km^2 (after 1996), depending on the method used.

Using the second dataset, which covers the past 36 years and incorporates the number of cars and vehicles in Modena as variables representing anthropogenic urban heat, the best predictor selected varies depending on the method and parameters applied. The predictors include A (urban area), C (CO_2 concentration), or the number of vehicles. Notably, regression trees identify new change points in the data for recent years. CHAID and exhaustive CHAID detect a shift in average temperature for $A > 40.8$ km^2 (Fig. 13), corresponding to years after 2007, or for $C > 398.8$ ppm (Fig. 14), corresponding to years after 2014. The latter change point is also identified by the C&RT algorithm (Fig. 15), in combination with the number of vehicles. For predicting the difference between local and global temperatures, all algorithms select local variables as the best predictors: A and V independently (Fig. 16) or A in combination with P (precipitation) (Fig. 17). The year when the difference becomes positive, indicating that local temperatures surpass global averages and the multivariate relationship with other variables shifts abruptly, is consistently identified as 1996 across all methods ($A > 37.98$ km^2, $A > 38.15$ km^2, or $V > 134{,}901$). These findings align with numerous studies that highlight the relationship between urbanization, urban heat (including heat generated by traffic congestion), and local warming in metropolitan areas worldwide (e.g. Tokairin et al. 2009; Mirzaei and Haghighat 2010; Arifwidodo and Chandrasiri 2015).

5 Conclusions

Climate change poses a significant threat to human safety and health through its impact on weather patterns. This study investigates changes in annual mean temperature and seeks to identify the key variables driving local temperature increases in urban environments, with the goal of prioritizing targeted adaptation actions. Two datasets are analyzed: the first spans 1881–2021 and includes local temperature, global CO_2 concentration, local precipitation depth, and local urbanization, while the second, covering 1986–2021, also incorporates the number of registered cars and vehicles in the area. Preliminary analyses of raw data and first differences reveal that linear relationships are spurious, likely due to shared positive trends across all variables except precipitation depth. To address this, advanced nonlinear and nonparametric statistical models, such as cubic splines and regression trees, are employed to examine the causes of local air temperature increases and the divergence between local and global temperature patterns. These methods provide average predictions that are not influenced by irregular fluctuations caused by specific internal climate variability.

The key findings of this study are as follows:

- Cubic splines and regression trees confirm that local urbanization and global CO_2 concentration are equally effective predictors of local temperature, shifting the focus to deviations between local and global temperatures (Figs. 9, 10, 13, and 14; Tables 1 and 3).
- The divergence between local and global temperatures, along with the faster warming observed locally, is best explained by local factors such as urbanization and the number of vehicles, either independently or in combination with local precipitation depth (Figs. 11, 12, and 15; Tables 2 and 4).
- Over the past 24 years (1996–2021), Modena has experienced a significant increase in local air temperature compared to the previous 120 years (1881–1995). The disparity between local and global temperature trends is primarily attributed to anthropogenic heat generated by urbanization and vehicular activity (Figs. 15, 16, and 17; Table 4).

These findings highlight the environmental impact of urbanization and vehicle-related heat effects, which extend beyond their well-known social, economic, and physicochemical consequences. Although further research is needed for reliable validation, an order-of-magnitude analysis confirms the plausibility of this hypothesis. The findings suggest that urban areas may experience a 'fever' from anthropogenic heat effects. Targeted mitigation strategies, such as reducing traffic congestion, could help address these localized impacts.

Appendix 1: Monthly local temperature

Figure 18 presents monthly values of local temperature (January–December), highlighting differences between the temperature in each month and global (*G*) and local (*T*) annual air temperatures. Although significant internal variability exists in local air temperature on a monthly scale, the long-term trends of *T*, *G*, and monthly values of *T* are similar. A detailed wavelet analysis of the dynamics of local changes, the timescales of the periodic components, and the local trends of monthly values of *T* and *P*, can be found in Morlini et al. (2023).

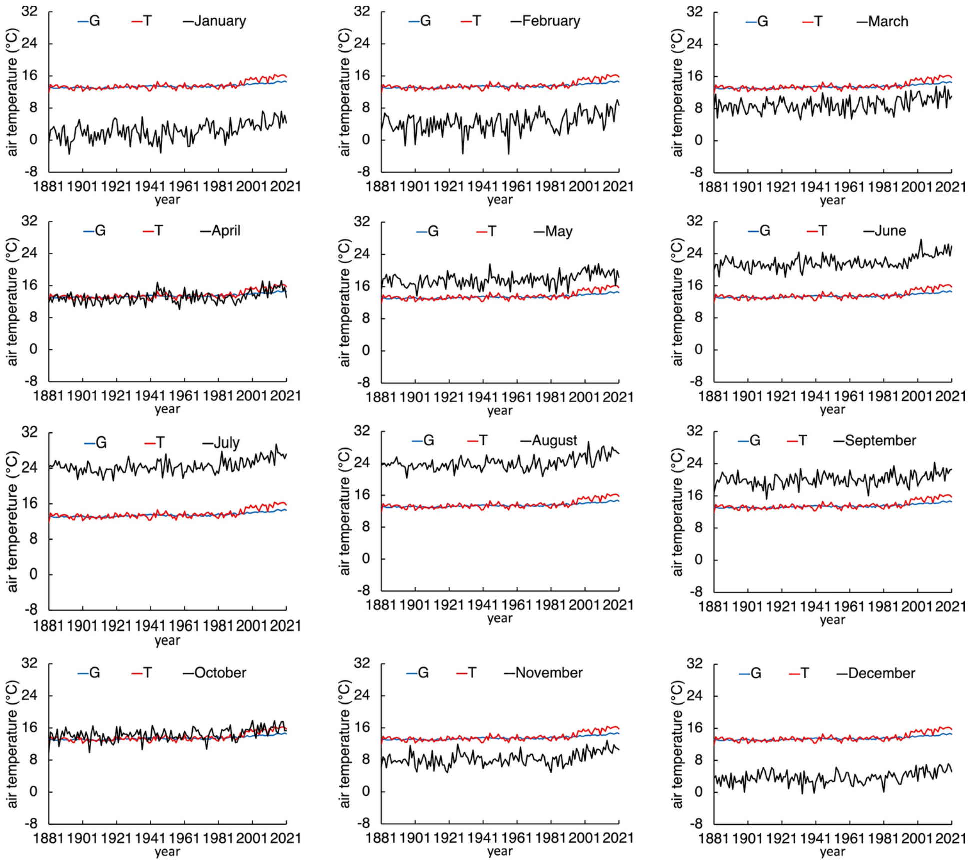

Fig. 18 Comparison of monthly (January–December) and annual local air temperature values observed in Modena (*T*) with NASA GISTEMP global (G) air temperature estimates from the Goddard Institute for Space Studies (GISS, *G*)

Appendix 2: NASA GISTEMP land & ocean combined

The NASA GISTEMP series used in this study was obtained from the official GISTEMP data portal (https://data.giss.nasa.gov/gistemp/) by selecting the Global Mean Temperature Land & Ocean Combined dataset (ASCII file GLB.Ts+dSST.txt). At least for the purposes of this study, this series does not significantly differ from the one obtained by selecting the Land-Only Temperature dataset (ASCII file GLB.Ts.txt), as shown in Fig. 19. The GISTEMP *G* series represents the global average temperature and, therefore, does not account for the fact that land surfaces warm faster than seas and oceans due to differences in thermal inertia, nor does it consider that different regions of the Earth warm at different rates. However, the close match between global and local temperatures during the period 1880–1990 suggests that regional differences relative to the global GISTEMP do not play a significant role, at least in determining local deviations from the global mean annual air temperature, as analyzed in this study. The visual comparison between the GISTEMP Land & Ocean combined series and the GISTEMP Land-only series confirms that differences in thermal inertia do not play a significant role in explaining the local deviations observed in the last two decades.

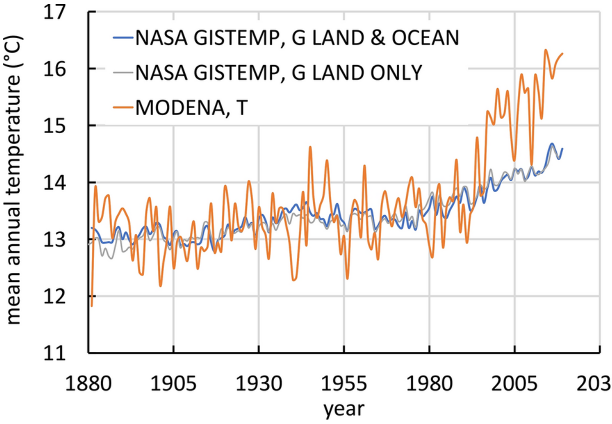

Fig. 19 Comparison between NASA GISTEMP global air temperature (*G* Land & Ocean Combined) and GISTEMP global air temperature (*G* Land Only) estimated by the Goddard Institute for Space Studies (GISS). Local air temperature observed in Modena (*T*) is also reported. GISTEMP global air temperature series for Modena are obtained by adding the average temperature observed in Modena in the 1951–1980 base period, namely $T_b = 13.38$ °C, to GISTEMP anomaly data

Appendix 3: Gridded NASA GISTEMP data

The NASA GISTEMP series used in this study was obtained from the official GISTEMP data portal (https://data.giss.nasa.gov/gistemp/) by selecting the Global Mean Temperature Land & Ocean Combined dataset (ASCII file: GLB.Ts+dSST.txt). This series is compared with another derived from 1° × 1° gridded data, also available through the GISTEMP portal (https://data.giss.nasa.gov/pub/gistemp/, NetCDF file: gistemp1200_GHCNv4_ERSSTv5.nc), as shown in Fig. 20. Modena, located at 44.65° N and 10.92° E, falls within the grid cell centered at 45° N and 11° E. As expected, the absolute temperatures derived from the gridded GISTEMP anomaly data generally fall between the global GISTEMP series (*G*), which represents the global average, and the local air temperature observed in Modena (*T*). Because this study focuses on deviations of local temperature from the global mean annual air temperature, the global GISTEMP series is preferred over the gridded dataset, which inherently includes local effects.

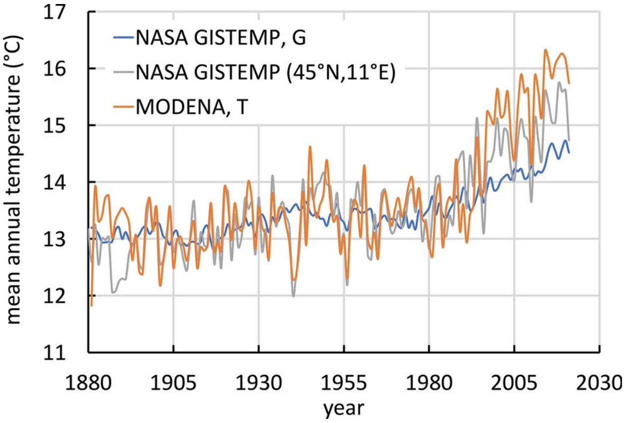

Fig. 20 Comparison between the NASA GISTEMP global air temperature (Land & Ocean Combined, *G*), the GISTEMP global air temperature for the 1° × 1° grid cell (45° N, 11° E) that includes Modena (44.65° N, 10.92° E), and the local air temperature observed in Modena (*T*). The GISTEMP global air temperature series for Modena is obtained by adding the average temperature observed in Modena during the 1951–1980 base period ($T_b = 13.38$ °C) to the GISTEMP anomaly data

Acknowledgements Air temperature and precipitation time series for Modena were provided by the Osservatorio Geofisico di Modena, Italy. The authors are grateful to Luca Lombroso for his specific comments and feedback on these data. This research was supported by Fondazione Cassa di Risparmio di Modena (Grant 2018-0093), the University of Modena and Reggio Emilia (Grant FAR 2020 Mission Oriented), and the European Union NextGenerationEU/NRRP, Mission 4 Component 2 Investment 1.5, Call 3277 (12/30/2021), Award 0001052 (06/23/2022), under the project ECS00000033 'Ecosystem for Sustainable Transition in Emilia-Romagna,' CUP E93C2200110001, Spoke 6 'Ecological Transition Based on HPC and Data Technology.' The authors thank Editor Salvatore Grimaldi the anonymous reviewers for comments that led to improvement in the manuscript.

Author contributions Isabella Morlini and Stefano Orlandini contributed to the conception and design of the study. Material preparation, data collection, and analysis were conducted by both authors. The first draft of the manuscript was written by Isabella Morlini and Stefano Orlandini, who also reviewed and commented on previous versions. All authors have read and approved the final manuscript.

Funding Open access funding provided by Università degli Studi di Modena e Reggio Emilia within the CRUI-CARE Agreement.
The authors have no relevant financial or non-financial interests to disclose.

Data availability Data sets used in this study are available from the authors upon request.

Declarations

Conflict of interest The authors declare no conflicts of interest relevant to this study and have no financial or non-financial interests to disclose.

References

Addinsoft (2023) XLSTAT: statistical and data analysis solutions. Addinsoft, New York, NY, USA. https://www.xlstat.com

Aldrich J (1995) Correlations genuine and spurious in Pearson and Yule. Stat Sci 10:364–376. https://doi.org/10.1214/ss/1177009870

Al-Sakkaf AS, Zhang J, Yao F et al (2024) Quantifying the stochastic trends of climate extremes over Yemen: a comprehensive assessment using ERA5 data. Stoch Environ Res Risk Assess 38:3639–3656. https://doi.org/10.1007/s00477-024-02772-6

Arifwidodo S, Chandrasiri O (2015) Urban heat island and household energy consumption in Bangkok, Thailand. Energy Procedia 79:189–194. https://doi.org/10.1016/j.egypro.2015.11.461

Armstrong B (2006) Models for the relationship between ambient temperature and daily mortality. Epidemiology 17:624–631. https://doi.org/10.1097/01.ede.0000239685.82829.62

Arnfield AJ (2003) Two decades of urban climate research: a review of turbulence, exchanges of energy and water, and the urban heat island. Int J Climatol 23:1–26. https://doi.org/10.1002/joc.859

Biggs D, De Ville B, Suen E (1991) A method of choosing multiway partitions for classification and decision trees. J Appl Stat 18:49–62. https://doi.org/10.1080/02664769100000005

Boccolari MA, Malmusi S (2013) Changes in temperature and precipitation extremes observed in Modena, Italy. Atmos Res 122:16–31. https://doi.org/10.1016/j.atmosres.2012.10.022

Breiman L, Friedman J, Olshen R, Stone C (1984) Classification and regression trees. Wadsworth & Brooks/Cole, Monterey

Brohan P, Kennedy JJ, Harris I, Tett SFB, Jones PD (2006) Uncertainty estimates in regional and global observed temperature changes: a new data set from 1850. J Geophys Res 111:D12106. https://doi.org/10.1029/2005JD006548

Buishand TA (1982) Some methods for testing the homogeneity of rainfall records. J Hydrol 58:11–27

Buishand TA (1984) Test for detecting a shift in the mean of hydrological time series. J Hydrol 73:51–69

Cardona-Jiménez J, Aguirre CAP, Gomez-Miranda IN et al (2024) Bayesian dynamic models to estimate the impact of halting vehicle fleets on the air quality: a case study from Medellín, Colombia. Stoch Environ Res Risk Assess 38:4331–4346. https://doi.org/10.1007/s00477-024-02806-z

Chauhan A, Singh RP (2020) Decline in PM2.5 concentrations over major cities around the world associated with COVID-19. Environ Res 187:109634. https://doi.org/10.1016/j.envres.2020.109634

Chen Y, Jiang WM, Zhang N, He XF, Zhou RW (2009) Numerical simulation of the anthropogenic heat effect on urban boundary layer structure. Theor Appl Climatol 97:123–134. https://doi.org/10.1007/s00704-008-0054-0

Chen X, Yang J, Zhu R, Wong MS, Ren C (2021) Spatiotemporal impact of vehicle heat on urban thermal environment: a case study in Hong Kong. Build Environ 205:108224. https://doi.org/10.1016/j.buildenv.2021.108224

Corradini E (2014) From the geophysical-meteorological observatory of Modena to the Italian network of observatories. In: Proceedings of the 12th conference of the International Committee of ICOM for University Museums and Collections (UMAC), Singapore, 10–12 October 2012. https://doi.org/10.18452/8741

De Munck C, Pigeon G, Masson V, Meunier F, Trémeac PB, Merchat M et al (2013) How much can air conditioning increase air temperatures for a city like Paris, France? Int J Climatol 33:201–227. https://doi.org/10.1002/joc.3415

Etheridge DM, Steele LP, Langenfelds RL, Francey RJ (1998) Historical CO_2 record derived from a spline fit (20-year cutoff) of the Law Dome DE08 and DE08-2 ice cores. Carbon Dioxide Information Analysis Center, Oak Ridge National Laboratory, U.S. Department of Energy. https://cdiac.ess-dive.lbl.gov/trends/co2/lawdome-data.html

Friedman J, Hastie T, Tibshirani R (2001) The elements of statistical learning. Springer, New York. https://doi.org/10.1007/978-0-387-21606-5

GISTEMP Team (2021) GISS surface temperature analysis (GISTEMP), version 4. NASA Goddard Institute for Space Studies. Dataset accessed 2022-11-25 at https://data.giss.nasa.gov/gistemp/

Gualtieri G, Brilli L, Carotenuto F, Vagnoli C, Zaldei A, Gioli B (2020) Quantifying road traffic impact on air quality in urban areas: a COVID-19-induced lockdown analysis in Italy. Environ Pollut 267:115682. https://doi.org/10.1016/j.envpol.2020.115682

Hansen J, Johnson D, Lacis A, Lebedeff S, Lee P, Rind D, Russell G (1981) Climate impact of increasing atmospheric carbon dioxide. Science 213:957–966. https://doi.org/10.1126/science.213.4511.957

Hansen J, Ruedy R, Sato M, Lo K (2010) Global surface temperature change. Rev Geophys 48:RG4004. https://doi.org/10.1029/2010RG000345

Harrell FE Jr (2015) Regression modeling strategies: with applications to linear models, logistic and ordinal regression, and survival analysis. Springer, New York. https://doi.org/10.1007/978-3-319-19425-7

Hastie TJ, Tibshirani R (1986) Generalized additive models. Stat Sci 1:297–310. https://doi.org/10.1214/ss/1177013604

Hausfather Z, Menne MJ, Williams CN, Masters T, Broberg R, Jones D (2013) Quantifying the effect of urbanization on U.S. Historical Climatology Network temperature records. J Geophys Res Atmos 118:481–494. https://doi.org/10.1029/2012JD018509

Hooker RH (1905) On the correlation of successive observations illustrated by corn prices. J R Stat Soc A 68:696–703. https://doi.org/10.2307/2339422

Jones PD, New M, Parker DE, Martin S, Rigor IG (1999) Surface air temperature and its changes over the past 150 years. Rev Geophys 37:173–199. https://doi.org/10.1029/1999RG900002

Jouzel J, Masson-Delmotte V, Cattani O, Dreyfus G, Falourd S, Hoffmann G et al (2007) Orbital and millennial Antarctic climate variability over the past 800,000 years. Science 317:793–797. https://doi.org/10.1126/science.1141038

Kass GV (1980) An exploratory technique for investigating large quantities of categorical data. J R Stat Soc C Appl Stat 29:119–127. https://doi.org/10.2307/2986296

Lenssen N, Schmidt G, Hansen J, Menne M, Persin A, Ruedy R, Zyss D (2019) Improvements in the GISTEMP uncertainty model. J Geophys Res Atmos 124:5919–6649. https://doi.org/10.1029/2018JD029522

Lenssen N, Schmidt GA, Hendrickson M, Jacobs P, Menne MJ, Ruedy R (2024) A NASA GISTEMPv4 observational uncertainty ensemble. J Geophys Res Atmos 129:e2023JD040179. https://doi.org/10.1029/2023JD040179

Lüthi D, Floch ML, Bereiter B, Blunier T, Barnola JM, Siegenthaler U et al (2008) High-resolution carbon dioxide concentration record 650,000–800,000 years before present. Nature 453:379–382. https://doi.org/10.1038/nature06949

Milly PCD, Betancourt J, Falkenmark M, Hirsch RM, Kundzewicz ZW, Lettenmaier DP, Stouffer RJ (2008) Stationary is dead: whither water management? Science 319:573–574. https://doi.org/10.1126/science.1151915

Mirzaei PA, Haghighat F (2010) Approaches to study urban heat island: abilities and limitations. Build Environ 45:2192–2201. https://doi.org/10.1016/j.buildenv.2010.04.001

Morgan JN, Sonquist JA (1963) Problems in the analysis of survey data, and a proposal. J Am Stat Assoc 58:415–434

Morlini I, Franco Villoria M, Orlandini S (2023) Modeling local climate change using site-based data. Environ Ecol Stat 30:205–232

Morlini I, Albertson S, Orlandini S (2024) Characterization of annual urban air temperature changes with special reference to the city of Modena: a comparison between regression models and a proposal for a new index to evaluate relationships between environmental variables. Stoch Environ Res Risk Assess 38:1163–1178

National Oceanic and Atmospheric Administration (NOAA) (2021) Trends in atmospheric carbon dioxide. NOAA Global Monitoring Laboratory. https://gml.noaa.gov/ccgg/trends/

Nunez M, Oke TR (1977) The energy balance of an urban canyon. J Appl Meteorol Climatol 16:11–19. https://doi.org/10.1175/1520-0450(1977)016%3c0011:TEBOAU%3e2.0.CO;2

Oke TR (1988) The urban energy balance. Prog Phys Geogr 12:471–508. https://doi.org/10.1177/030913338801200401

Oke TR, Mills G, Christen A, Voogt JA (2017) Urban climates. Cambridge University Press, Cambridge

Perperoglou A, Sauerbrei W, Abrahamowicz M, Schmid M (2019) A review of spline function procedures in R. BMC Med Res Methodol 19:66. https://doi.org/10.1186/s12874-019-0666-3

Qian L, Jin G, Wang C et al (2024) A new method for detecting abrupt changes in the dependence among multivariate hydrological series based on moving cut total correlation. Stoch Environ Res Risk Assess 38:467–488. https://doi.org/10.1007/s00477-023-02580-4

Rachma ST, Lin YC (2024) Investigating the changing spatiotemporal urban heat island and its impact on thunderstorm patterns by Hilbert Huang transform. Stoch Environ Res Risk Assess 38:263–280. https://doi.org/10.1007/s00477-023-02571-5

Rao Y, Liang S, Yu Y (2018) Land surface air temperature data are considerably different among BEST-LAND, CRU-TEM4v, NASA-GISS, and NOAA-NCEI. J Geophys Res Atmos 123:5881–5900. https://doi.org/10.1029/2018JD028355

Ritschard G (2013) CHAID and earlier supervised tree methods. In: McArdle JJ, Ritschard G (eds) Contemporary issues in exploratory data mining in the behavioral sciences. Routledge, New York, pp 48–74

Rizwan AM, Dennis LYC, Liu C (2008) A review on the generation, determination and mitigation of urban heat island. J Environ Sci 20:120–128. https://doi.org/10.1016/S1001-0742(08)60019-4

Salamanca F, Georgescu M, Mahalov A, Moustaoui M, Wang M (2014) Anthropogenic heating of the urban environment due to air conditioning. J Geophys Res Atmos 119:5949–5965. https://doi.org/10.1002/2013JD021225

Stoica P, Selen Y (2004) Model-order selection: a review of information criterion rules. IEEE Signal Process Mag 21:36–47. https://doi.org/10.1109/MSP.2004.1311138

Sutton R, Suckling E, Hawkins E (2015) What does global mean temperature tell us about local climate? Philos Trans R Soc A 373:20140426. https://doi.org/10.1098/rsta.2014.0426

Taylor JR (1997) An introduction to error analysis: the study of uncertainties in physical measurements. University Science Books, Sausalito

Tokairin T, Sofyan A, Kitada T (2009) Numerical study on temperature variation in the Jakarta area due to urbanization. In: Proceedings of the 7th international conference of urban climate, vol 5, pp 3–6

Trevin LV (2016) Global observed long-term changes in temperature and precipitation extremes: a review of progress and limitations of IPCC assessments and beyond. Weather Clim Extrem 11:4–16. https://doi.org/10.1016/j.wace.2015.10.002

Wood SN (2017) Generalized additive models: an introduction with R. Chapman & Hall/CRC, Boca Raton

Wu J, Shen J, Zhang X, Skitmore M, Lu W (2016) The impact of urbanization on carbon emissions in developing countries: a Chinese study based on the U-Kaya method. J Clean Prod 135:589–603. https://doi.org/10.1016/j.jclepro.2016.06.121

Yu Z, Hu L, Sun T, Albertson J, Li Q (2021) Impact of heat storage on remote-sensing based quantification of anthropogenic heat in urban environments. Remote Sens Environ 262:112520. https://doi.org/10.1016/j.rse.2021.112520

Zittis G, Almazroui M, Alpert P, Ciais P, Cramer W, Dahdal Y et al (2022) Climate change and weather extremes in the Eastern Mediterranean and Middle East. Rev Geophys 60:e2021RG000762. https://doi.org/10.1029/2021RG000762